NASA Contractor Report 4674

The Determination of the Constitutive Parameters of a Medium With Application to a Reinforced Concrete Pad

A. J. Poggio, G. J. Burke, and S. T. Pennock

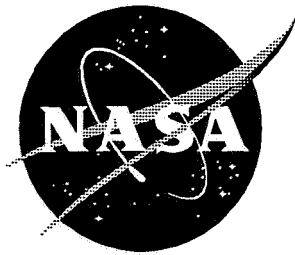# The Determination of the Constitutive Parameters of a Medium With Application to a Reinforced Concrete Pad

A. J. Poggio, G. J. Burke, and S. T. Pennock
Lawrence Livermore National Laboratory • Livermore, California

CONTENTS

Acknowledgment

The authors are grateful to a number of individuals for their support during the performance of the experimental program. The Test Director was Ly Dao of USAF Phillips Laboratory and the experimental operations team, led by John Millard of United International Engineering Inc., included James Tucker of UIE.

This effort was part of the NASA Low Power On-the-Ground Test portion of the NASA Boeing 757 HIRF Tests under Project Manager Charles Meissner. This, in turn, was part of the NASA Fly-By-Light/Power-by-Wire Program.

1. Introduction

This report describes the experimental and analytical program performed to determine the constitutive parameters of the reinforced concrete pad in the test facility used during the Low Power On-the-Ground portion of the NASA Boeing 757 HIRF Tests [1]. These tests were conducted during the period September 20 to October 21, 1994 in the LESLI facility at the Phillips Laboratory, Kirtland AFB, NM.

The on-the-ground tests were designed to meet several objectives including support of a flight test series and the generation of data for the validation of codes and models that could be used to predict the electromagnetic environment in transport aircraft. To satisfy these objectives, tests were to be executed in a known environment and the data compared to modeling results. A critical feature of this testing was the "known environment" which implies knowledge of the parameters which are critical to an effective modeling activity and which could include, among many other things, definitions of the airplane and its physical and electrical configuration, the ground upon which it sits when stationary, the fields impinging on the aircraft, and the radiating or bounding structure in the simulator. We would want to specify the electromagnetic characteristics of the entire space that would likely enter into a mathematical modeling effort so that the model can be made as "close" to physical reality as desired prior to exercising computational algorithms which might introduce their own uncertainties.

Since we are evaluating codes used for determination of the electromagnetic environment in aircraft and since the on-the-ground test involved an airplane parked on a pad in the simulator facility, we would require a definition of the constitutive parameters of the pad. Initially, the test plan called for the pad to be partially covered by a highly conducting covering composed of interconnected aircraft landing mats with a total surface area in excess of 15,000 ft^2. Difficulties associated with timely delivery of the mats, installation of the panels on the pad, and uncertainties in the quality of the electrical interconnection of the individual panels prevented use of these panels and required situation of the airplane on the bare, reinforced concrete pad. As a result, the need for measurement of the constitutive parameters of the LELSI concrete pad arose.

4

The evaluation of the constitutive parameters was performed under a number of significant constraints that served to restrict the available options. The constraints were:

- In order to limit costs, the measurement process was to be minimized in time extent without severely compromising the quality of the data

- The measurement process was limited by the availability of the experimental system including the RF sources and the data acquisition system. Ultimately, this limitation confined the pad characterization tests to a one-week period including assembly and disassembly of the test fixtures and equipment, testing and dry runs of the entire system, equipment down-time, and actual acquisition runs for the data.

- Construction details for the pad, constructed over 40 years ago, were not available. Thus, reinforcing rod location, concrete thickness and specifications were unknown.

- The measurement techniques were to be completely noninvasive, namely, the pad could not be cored or probes emplaced below the surface.

- The RF equipment and the data acquisition team's experience in performing ground parameter measurements were somewhat limited. Accurate reflection angle, scattering and polarization measurements as might be required in Brewster angle and wave tilt measurements were possibly beyond the capabilities of the available equipment.

Since the precise detailed structure of the pad is unknown and since a detailed spatial description of the constitutive parameters is not required for the purposes of the code validation exercise in view of the level of precision with which other environmental descriptors are known, a technique which averages material characteristics over some spatial extent has been deemed adequate. In view of these observations, the constraints above, and discussions with experts in this technical area such as Drs. Ray King and George Hagen, a method based on wave propagation along wires closely coupled to the ground structure was chosen. The remainder of this report describes the test and analyses involved in determining the constitutive parameters. In the analysis, arguments are made regarding the adequacy of the quality of the results insofar as their role in the code validation exercise is concerned. It would not be reasonable to expend inordinate resources to greatly reduce uncertainties in the parameters when the uncertainties might only be reflected as second order effects. But, realizing the potential value of this scheme for the determination of constitutive parameters in general situations, some concerns and suggestions for future work are presented.

2. Proposed Approach

The method chosen for the determination of the constitutive parameters is based on the theoretical solution for current propagation on a wire above a homogeneous half-space with arbitrary permittivity ε, and conductivity σ. For the purposes of this study, the permeability μ of both half spaces (above and below the ground plane) will be assumed equal to that of free space μ_o. A solution for the current distribution on an infinitely long wire over ground, with no limitations on the ground constants, has been developed by Chang, Olsen and Kuester [2, 3, 4]. Their analysis leads to a modal expansion of the current on the infinitely long wire in which they found two discrete modes and continuous spectrum components associated with radiation. One of the discrete modes is referred to as the structure attached or transmission line mode, is dominant near the source on a wire close to the ground, and is a slow wave in the case of conducting grounds. The other discrete mode exhibits fast wave characteristics, has substantially less attenuation along the direction of the wire than does the transmission line mode, and is mainly important for large heights above ground.

2.1 Solutions for a Wire Over Ground

In [2], with time variation $\exp[-i\omega t]$, an integral equation for the current on an infinite horizontal wire along the x axis, with radius a and height $z = h$ over a ground plane, is solved for a delta-function source located at $x = 0$. The solution for the current is

$$I(x) = \frac{2}{\pi\zeta_o} \int_{-\infty}^{\infty} \frac{\exp(ikx\gamma)}{M(\gamma)} d\gamma \tag{1}$$

where $M(\gamma)$ is the Fourier transform of the integral equation kernel and $k = (\mu_0\varepsilon_0)^{1/2}$, is the propagation constant in the upper half-space. For a perfectly conducting wire, $M(\gamma)$ is [4]

$$M(\gamma) = \zeta^2\left[H_o^{(1)}(\zeta A) - J_o(\zeta A)H_o^{(1)}(2\zeta H)\right] + P(\gamma, 2H) - \gamma^2 Q(\gamma, 2H) \tag{2}$$

where $H = kh$ and $A = ka$, and $\zeta = \left(1 - \gamma^2\right)^{1/2}$ with $\text{Im}\,\zeta \geq 0$. The functions P and Q are given by the integrals

$$P(\gamma, Z) = \frac{2}{i\pi} \int_{-\infty}^{\infty} \frac{e^{-u_1 Z}}{u_1 + u_2} d\lambda \qquad\qquad Q(\gamma, Z) = \frac{2}{i\pi} \int_{-\infty}^{\infty} \frac{e^{-u_1 Z}}{n^2 u_1 + u_2} d\lambda \tag{3}$$

6

where $n = \left(\varepsilon_r + i\sigma / \omega\varepsilon_0 \right)^{1/2}$ for ε_r and σ the relative dielectric constant and conductivity of the ground and

$$u_1 = \left(\lambda^2 - \zeta^2 \right)^{1/2}, \qquad u_2 = \left(\lambda^2 - \zeta_n^2 \right)^{1/2}, \qquad \mathrm{Re}\, u_1, u_2 \geq 0$$

$$\zeta_n = \left(n^2 - \gamma^2 \right)^{1/2}, \qquad \mathrm{Im}\, \zeta_n \geq 0.$$

The current in Equation (1) is represented as a spectrum of exponential waves with a propagation constant $k\gamma$. However, if the integration contour is deformed into the complex γ plane, the current is found to be composed of one or two discrete modes at poles of the integrand where $M(\gamma) = 0$ and three branch cut integrals [4]. For the wire height and frequencies considered here, the important components are a discrete mode with $\gamma = \gamma_p$, where $M(\gamma_p) = 0$, and a branch cut integral from $\gamma = 1$. This discrete mode has the character of an attenuating slow wave and is called the transmission line mode. The component of current in this mode is given by the residue at the pole as

$$I_p(x) = 4i(\mu_0\varepsilon_0)^{-1/2} \exp(ik\gamma_p x) / M'(\gamma_p) \tag{4}$$

There can be a second discrete mode, known as the surface-attached mode, which has the nature of a fast wave, but it does not appear significant in the case of our measurements. The branch cut integral yields a component of current with asymptotic form $\exp(ikx)/x^2$, so it is important very near the source but it quickly drops below the transmission line mode. However, at some larger distance the exponential decay of the transmission line mode will always take it below the branch cut term which is decreasing algebraically. Hence, there is a window in x where the transmission line mode is dominant, and this region is of primary interest in our measurements since information about the ground parameters is most easily extracted from γ_p.

In the typical forward solution for the discrete modes, the ground constants ε and σ are substituted into Equation (2) and the solution for $M(\gamma) = 0$ is found by numerical iteration. For the problem at hand, namely determination of ε_r and σ given the attenuation and phase constant for a measured current distribution on the wire, the inverse problem must be solved. Formally, for a given frequency, wire radius, and height above ground, α and β are determined by fitting the measured current $I(x)$. Then $\gamma_p = (\beta + i\alpha)/k$ is substituted for γ in Equation (2) and the equation is solved numerically for ε_r and σ. The final results are then the constitutive parameters for the pad at a set of frequencies (as many as desired).

2.2 The Physical Layout

The concrete pad that is the subject of this analysis is shown in Figure 1. The pad, which is approximately 94 meters in diameter, is composed of reinforced concrete with unknown structural characteristics. The source region is covered with an aluminum plate as shown, which measures approximately 20 meters from the edge of the pad to the triangular plates forming the transition region from aluminum to concrete. For the purposes of the characterization, one of the LESLI rhombic antenna wires was stretched, under some tension, across the pad and continued across the earth surroundings. The wire, with diameter 3/16 inches (radius = 0.238 cm), was approximately 200 meters in length with the portion beyond the 100 meter mark containing randomly placed loads in an attempt to suppress reflections when used in the rhombic configuration. In an attempt to isolate the wire from the pad over a considerable portion of its length, the wire was placed on a dielectric support. The closed cell Styrofoam support was composed of two strips each 1/4 inch thick and 8 inches wide to form a 1/2 inch by 8 inch support structure. The support was secured to the concrete with duct tape. A cross section view of the arrangement of the wire, Styrofoam support, aluminum plane, and concrete pad is shown in Figure 2. The Styrofoam support material was characterized using a network analyzer and a stripline fixture, and its relative dielectric constant was measured to be approximately 1.03 over the range of frequencies from 50 MHz to 1 GHz. The wire was tensioned with turnbuckles and secured to a stake beyond the edge of the concrete pad. The remainder of the wire, containing the randomly located loads, was allowed to remain on the ground in the random configuration it assumed when lowered to the ground. Cutouts were made in the Styrofoam support strip to accommodate the current probes. Ultimately, the axis of the wire was 5/8 inches (1.5875 cm) with an uncertainty of 1/8 inch above the ground plane. The current was measured with Prodyne I320 current probes that were connected to NanoFast high frequency fiber optic links by one-meter long coaxial cables that were orthogonal to the wire to minimize coupling and high frequency losses. The signals were routed to a fiber optic (F-O) receiver for optical to electrical conversion and then to an HP automatic network analyzer. Ultimately the network analyzer output was routed to a recording computer. The system is shown in Figure 3.

2.3 The Measurement Process

To execute the tests, the wire was driven against the aluminum ground plane and the current distribution was measured at selected points along the wire. From this measured
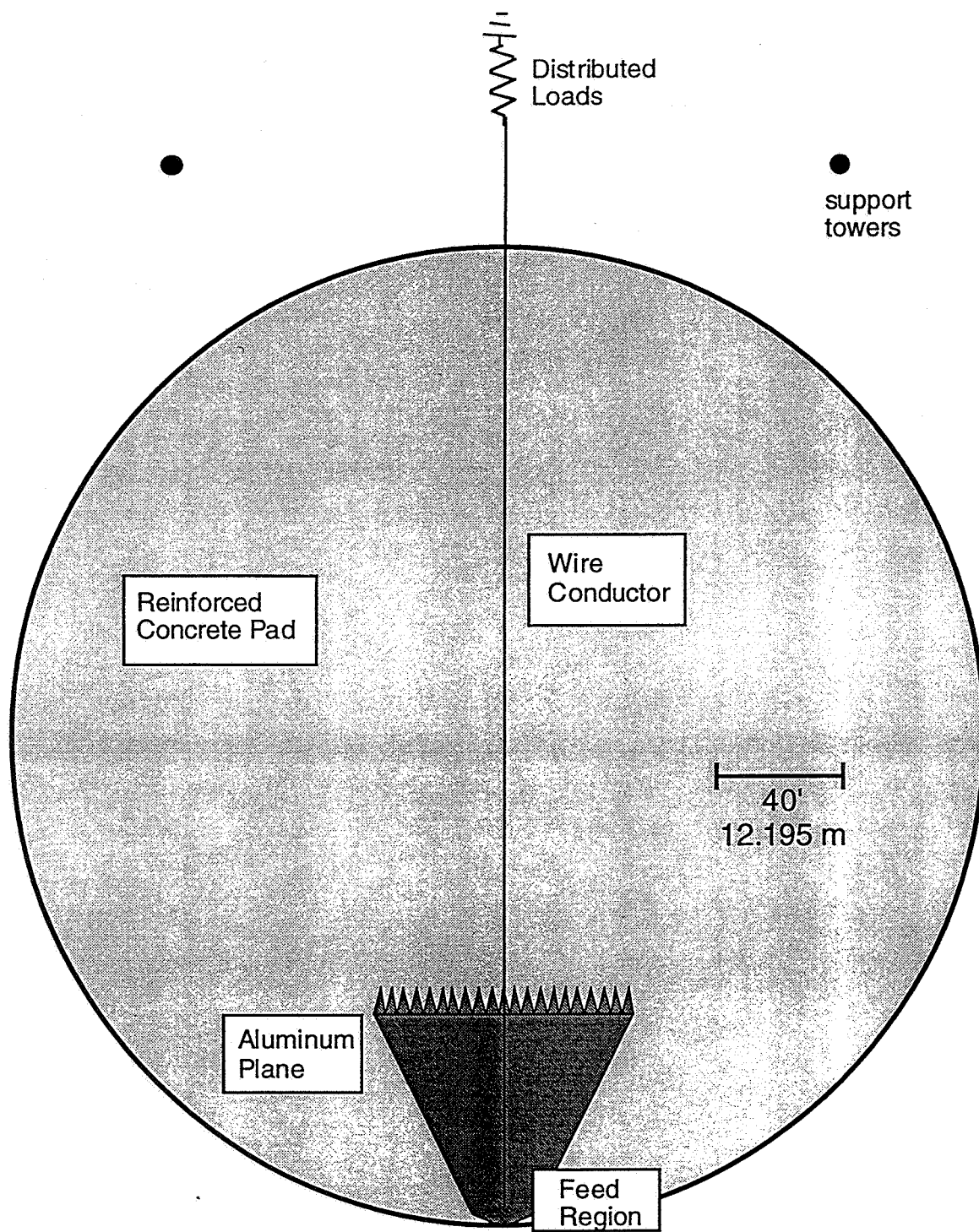
8
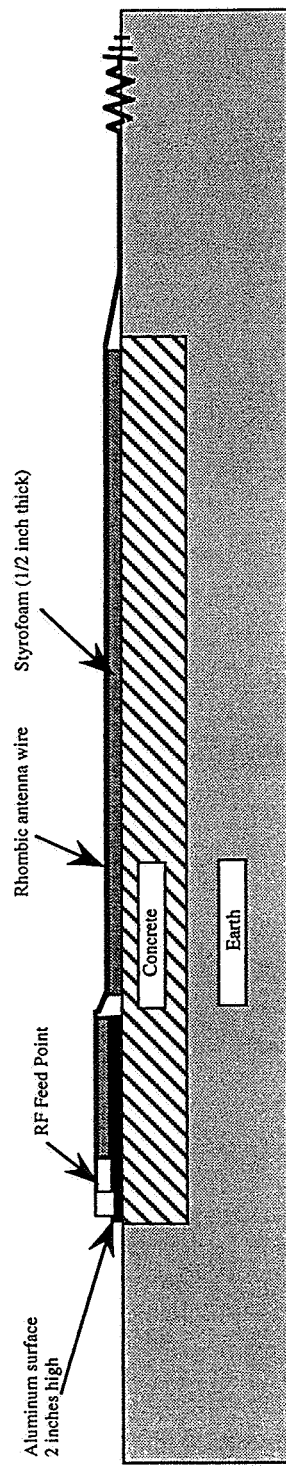
Figure 1. Pad characterization wire layout

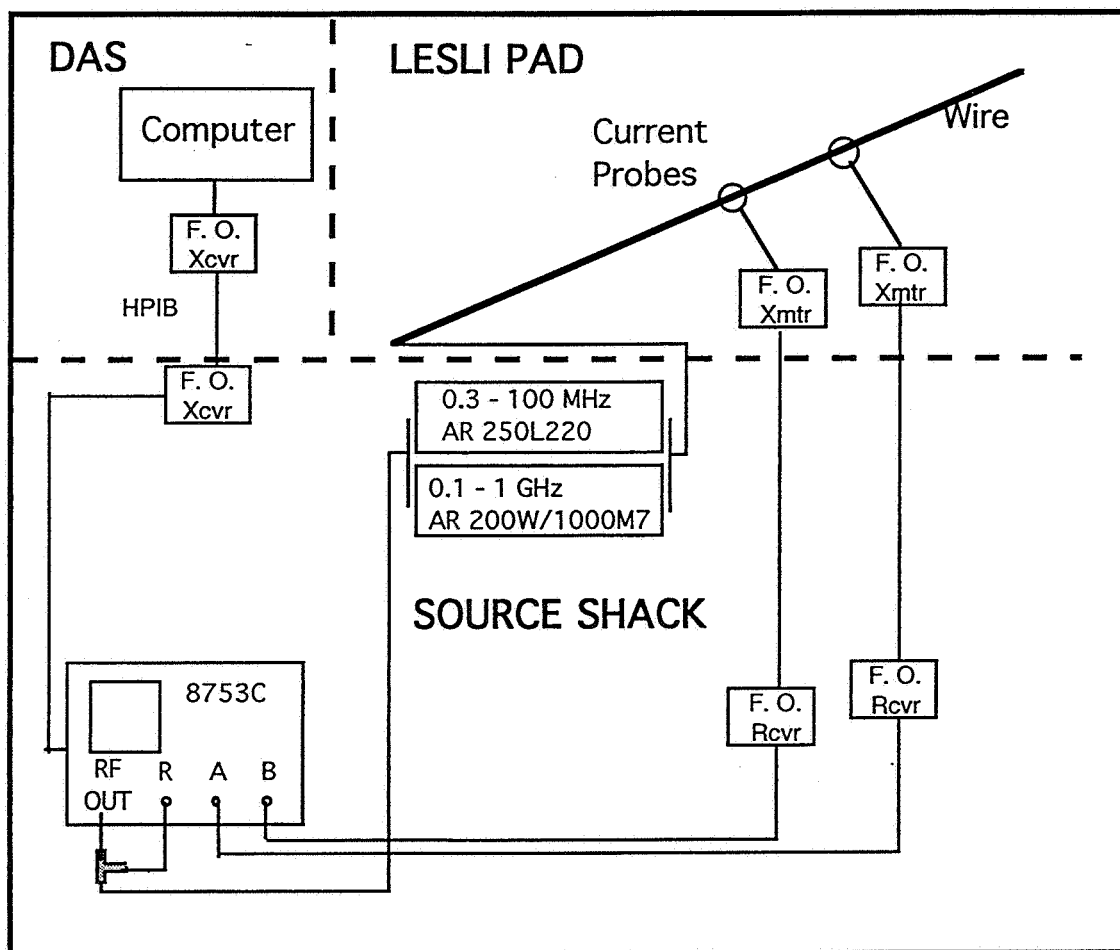Figure 2. Pad Characterization Wire Layout - Cross Sectional View

Figure 3. Ground characterization instrumentation

current distribution the attenuation and phase constants were determined using methods described later. The method used in data acquisition was to simultaneously measure the current at two points along the structure over the entire range of frequencies with one point (Point 1) always located at the first measurement site closest to the source, viz., $x = 22.5$ meters. For the purposes of this study, the frequency range was from approximately 1 MHz to approximately 1 GHz. Starting at a point 22.5 meters from the feed point on the aluminum plane that coincides with the rhombic apex, the current was measured at 30 cm intervals for a total of 90 points. The locations, with the reference probe at 22.5 meters (Point 1), are given by

$$x \text{ (meters)} = 22.5 + 0.3(n-1), \quad n = \{1,90\}$$

Based on the premise that the current distribution for a wire very close to the ground is dominated, especially near the source, by a complex exponential $\exp(ik\gamma x)$ with γ defined by zeroes of $M(\gamma)$ in the complex plane, it becomes clear that relative measurements of current are adequate for evaluation of attenuation and phase constants. For example, the ratio of current at Point n to the current at Point 1 when the currents are measured simultaneously, or are the results of identical source conditions at the feedpoint, is simply

$$I(x_n)/I(x_1) = \exp(ik\gamma(x_n - x_1)) \qquad (5)$$

Clearly the reference signal strength is normalized out of the analysis and evaluation of the attenuation and phase constant becomes straightforward, in principle. The data was collected by stepping through all frequencies of interest in a spatial-pairwise scheme [$I(x_n)$ and $I(x_1)$] for all n. Hence, we measure and store $I(x_n, \omega_j) / I(x_1,\omega_j)$, n = $\{2,90\}$, and j = $\{1,J\}$, i.e., we record the normalized current (as well as each component, in reality) at fixed positions for stepped frequency sweeps. Ultimately, we use this data in a different format, namely, we use the normalized current at fixed frequency for stepped position to determine α and β. The structure of this data matrix is represented graphically in Figure 4 where $I(x_i, \omega_j)$ is represented by I_{ij} and the data is acquired along columns (fixed position) and processed along rows (fixed frequency). This then allows the determination of the normalized attenuation and phase constants as a function of frequency. Using these, one then performs the inverse evaluation of the constitutive parameters as described later. Some uncertainties arise regarding this approach to the determination of the constitutive parameters. Namely, it is unknown, a priori, if this method is robust and unaffected by the presence of noise in the measured data. The literature abounds with non-robust methods for evaluation of the parameters in complex exponentials. In addition to the impact of measurement noise in the data, the impact of other uncertainties such as the importance of
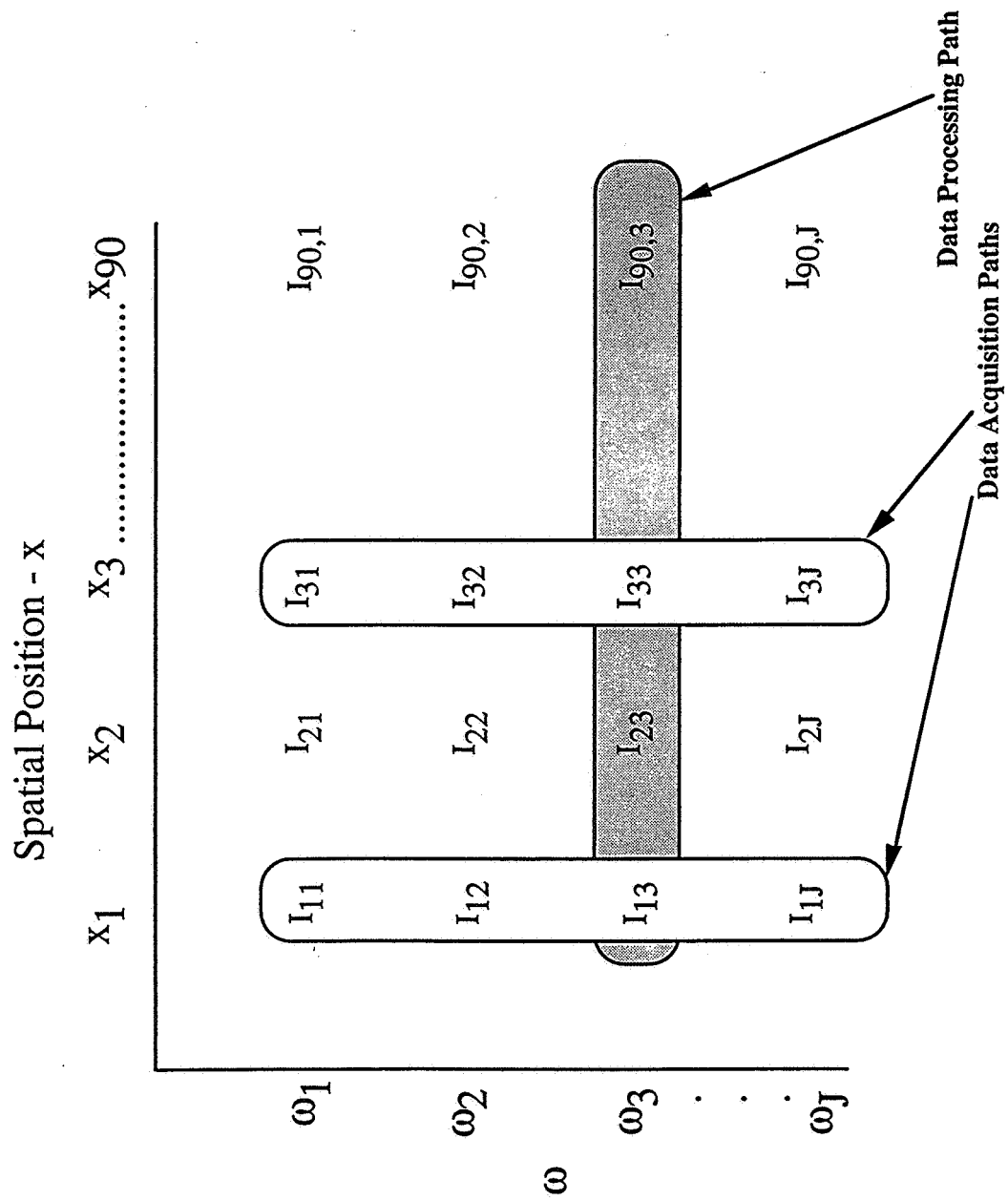
12

Figure 4. Data Acquisition and Processing Paths

13

precision in the height of the wire above the ground plane, is unknown. All these uncertainties could be corrected with some further work in which numerical testing is offered as a potential fix to this dilemma.

3. Experiment and Data

3.1 The Acquired Data

An example of the data, as acquired, is shown in Figure 5 for two points along the wire, namely, Point 1 (the reference) and Point 20. For fixed position, the data represent the spectrum of the current and the plot is an example of the vertical strip in Figure 4. During the acquisition phase, ninety such data records were generated, i.e., current as a function of frequency for fixed position. In order to remove the source strength from the data, the current magnitude was normalized to the reference current at Point 1 and such a result is shown in Figure 6. The poor data behavior beyond 250 MHz is due in large part to the signal level at Point 20 having fallen below the noise floor in the measurement system. In the vicinity of this anomalous behavior, the current at Point 20 was more than 60 dB below the current at Point 1. And, in this frequency range, the current at Point 1 had already fallen more than an order of magnitude below its value at low frequencies. These combined effects could easily drive the signal below the system measuring capabilities. Also, there are instances where the current at Point 20 exceeds that at Point 1. This can be due to uncertainties in the measurements or the presence of a standing wave on the structure.

For the purposes of data analysis, the records were processed to provide an additional set of records which portray the current as function of position for fixed frequency. This presentation is representative of the horizontal strip in Figure 4 and a visual example of the data for such a "strip" is shown in Figure 7. The data in Figure 7 exhibit a substantial amount of variation on a point to point basis thus leading to questions regarding the source of this structure in the current distribution. Observations were made that the peaks did not move with changes in frequency, thus ruling out a strong standing wave on the line as the cause for these peaks. An investigation was made of the possibility that perturbations and inclusions in the concrete in the vicinity of the peaks might cause the excursions. Visual inspection of the pad and a study of photographs of the pad with the wire in place did not provide an obvious clue as to the cause. The possibility of rebar-induced perturbations in
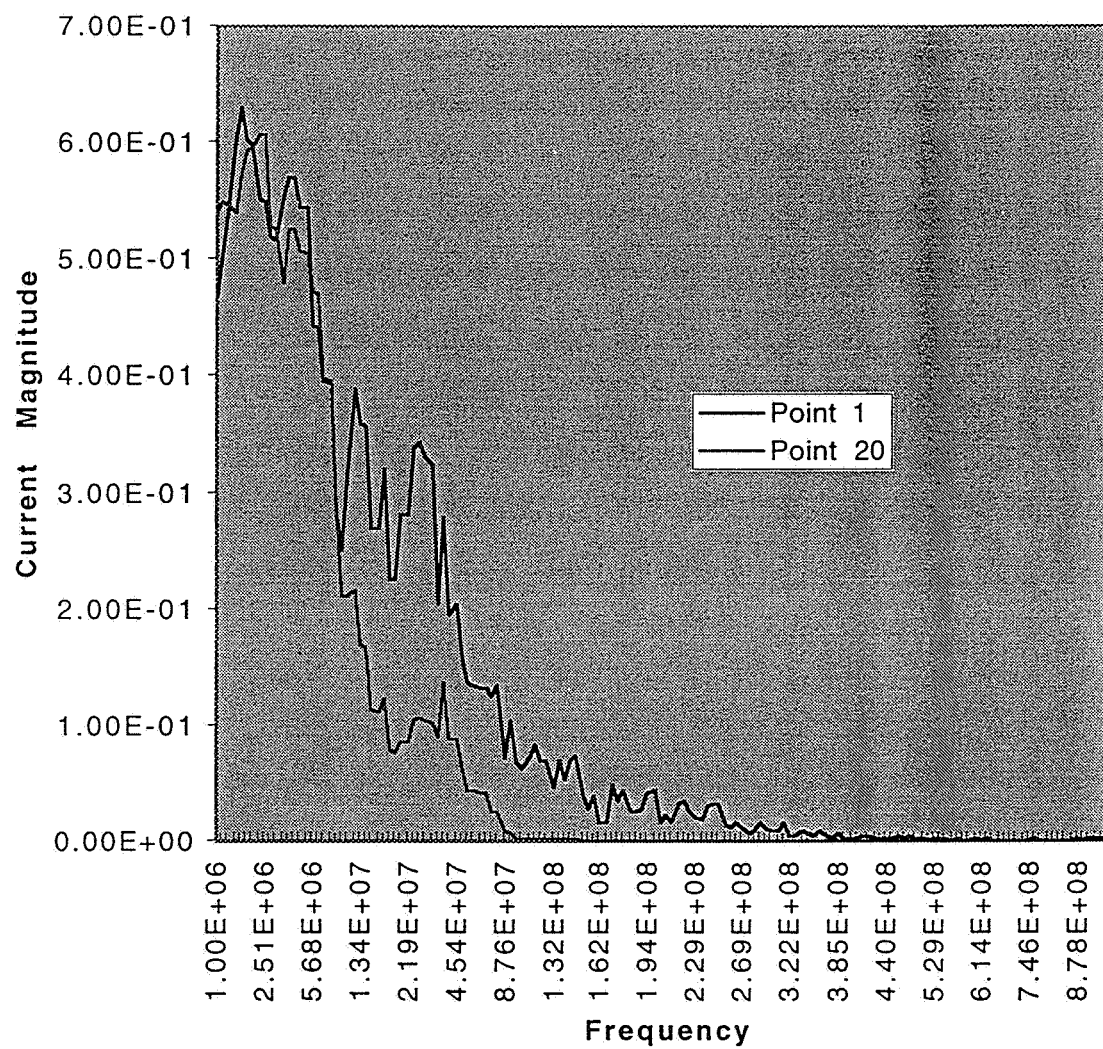
14

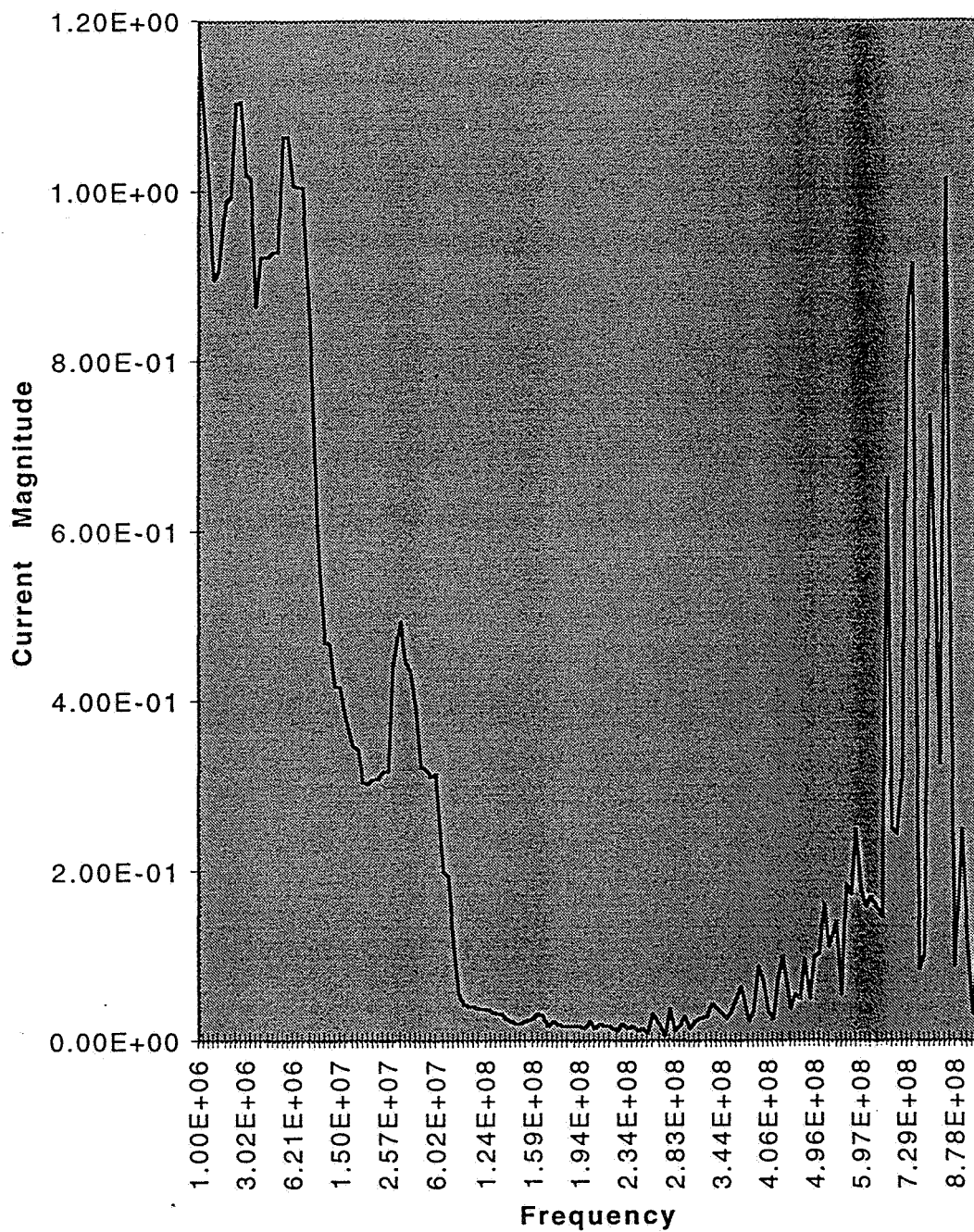Figure 5. Current magnitude spectrum at Points 1 and 20

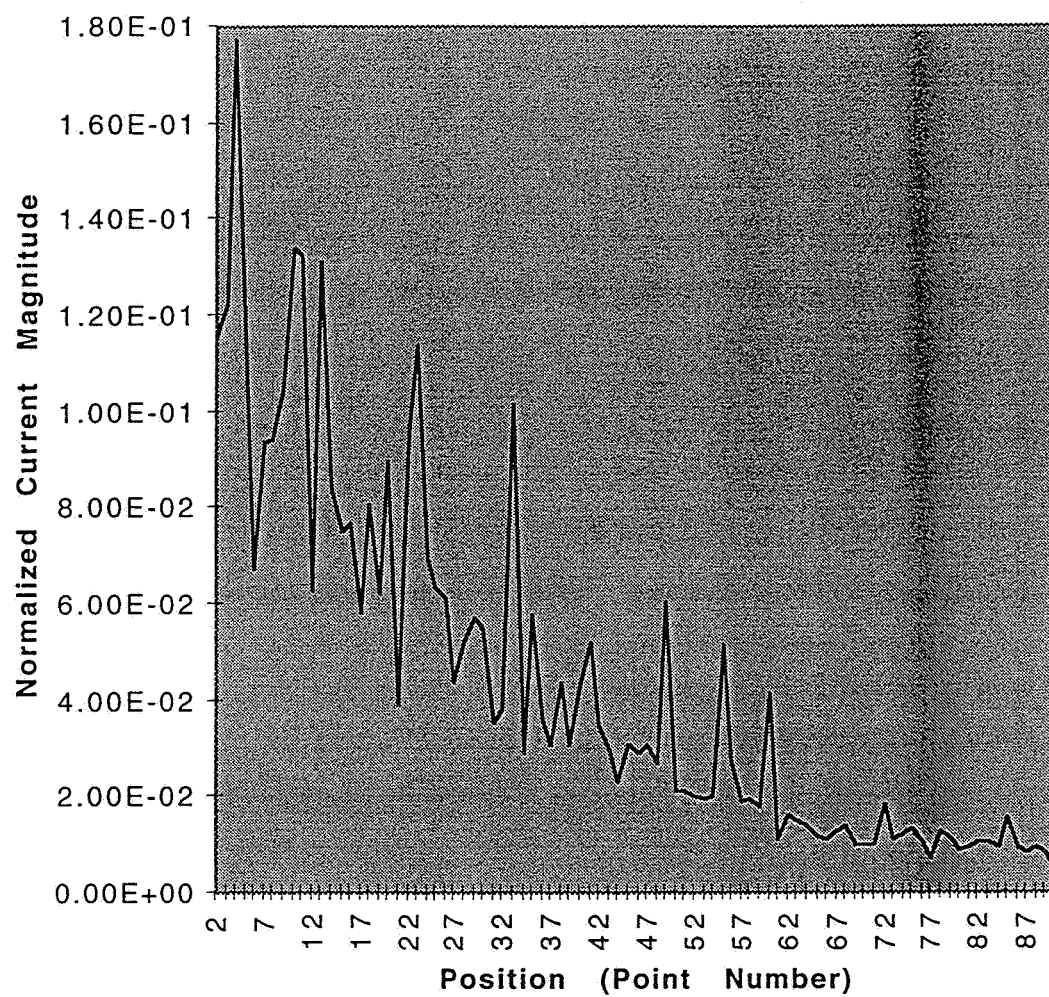Figure 6. Normalized current magnitude spectrum at Point 20

Figure 7 Normalized current as a function of position along the wire at 30 MHz

the fields and currents was also offered. However, modeling was performed using NEC [6] to analyze an end-driven wire very close (h=5/8 inches) to a ground ($\varepsilon_r = 6$, $\sigma = 0.006$ S/m) with a single strand of perfectly conducting rebar that was buried at six inches. The effects on the wire current distribution were negligible except when the wire and rebar were parallel and aligned in the vertical plane. In the parallel case, the current showed perturbations in the average values of α and β but nothing in its behavior as localized as seen in the measured data. Nothing could be detected which was capable of causing such a rapid change in current. Also, the pad was constructed of concrete squares and the wire was oriented diagonally across the squares. Given common concrete building practices, the rebar was most likely oriented parallel to the sides of the squares and orthogonal to edges so that it is unlikely that the rebar and wire were parallel. Other possibilities were considered, including measuring equipment malfunction.

A 3-D view of the data in the 10 to 275 MHz range over the sampled extent of the wire allows a visualization of the previous discussions and is shown in Figure 8. The spectral behavior of the current (without normalization), its spatial behavior and its decay rates in these two variables is evident. The presence of the "spikes" or peaks in the current as a function of position mentioned earlier is also evident. Note that the "spikes" occur at identical positions independent of frequency and manifest themselves in this figure as ridges or striations at a constant position coordinate. Since the data acquisition for a single run was effected at a fixed position with frequency stepped, an offset or malfunction throughout a run could manifest itself as a frequency independent perturbation at a fixed location. A few sources of such error were considered. A malfunctioning or improperly placed or configured current probe could produce such perturbations. The current probes were of the "clothespin" type, that is, they were spring-loaded clamps that fit around the wire. These were repositioned for each run with only the reference at Point 1 unperturbed during the data acquisition process. Another possibility was inadvertent or improperly applied attenuators in the fiber optic link.[1] Such a situation could be realized if the stepping attenuator system which was electronically controlled was sporadically "sticking" and reporting an incorrect value to the data acquisition system. At the present time, the identification of the source of the variability of the data has not been successful.

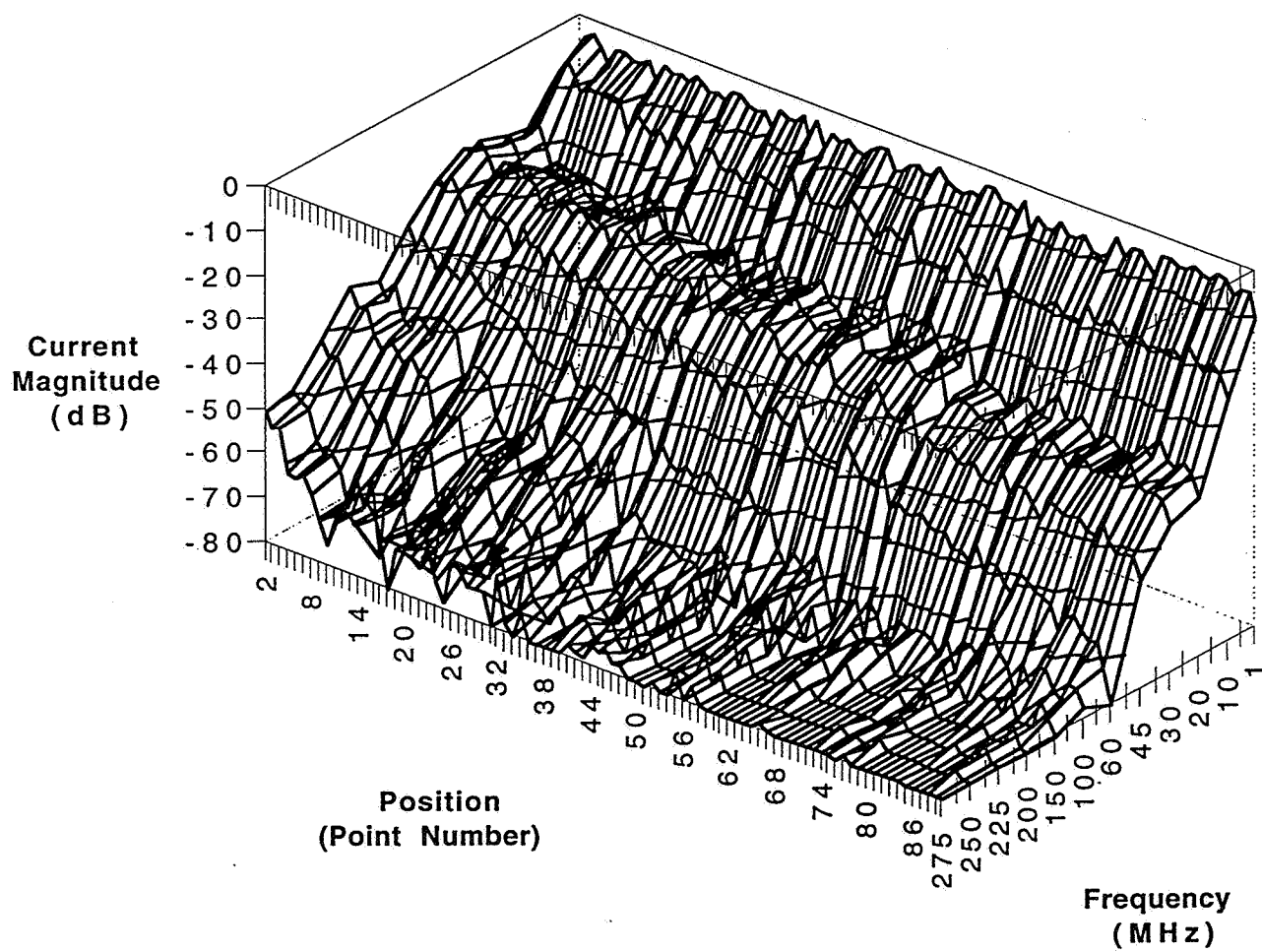[1] J. H. Millard, Private Communication

18

Figure 8. Magnitude of current on the wire as a function of position and frequency

19

3.2 Extraction of Attenuation and Phase Constants

As explained in Section 2.1, the component of current of diagnostic value is the transmission line mode which is dominant in a window from the source to a point where it drops below the branch cut mode. Hence, we need to locate this region on the wire and estimate the attenuation and phase constants. Given that the current can be represented by

$$I(x,\omega) = I_0 \exp\left[i(\beta(\omega) + i\alpha(\omega))(x - x_1)\right] \;,\; k\gamma = \beta + i\alpha \qquad (6)$$

an exponential fit to the acquired data (or a normalized version of the data) or a linear fit to the log of the data can provide values for the normalized attenuation and phase constants. Using the complex natural logarithm of the data, one has

$$-[\alpha(\omega) - i\beta(\omega)](x - x_1) + Ln(I_0) = Ln(I(x,\omega)) \qquad (7)$$

so that, for two points along the structure at x_i and x_j at a fixed frequency ω_n, one can solve for $\alpha(\omega_n)-i\beta(\omega_n)$

$$\alpha(\omega_n) - i\beta(\omega_n) = [Ln(I(x_i, \omega_n)) - Ln(I(x_j, \omega_n))] / (x_j - x_i) \qquad (8)$$

Keep in mind that these are complex natural logs. Using the real and imaginary parts of the equation with the current represented by $|I(x,\omega)|\exp(j\phi(x,\omega))$, with $\phi(x,\omega)$ the phase at x and ω, it is a simple matter to extract $\alpha(\omega_n)$ and $\beta(\omega_n)$ and present them in common log notation thus allowing easy conversion to a dB scale

$$\alpha(\omega_n) = 2.3025 \,[\log|I(x_i, \omega_n)| - \log|I(x_j, \omega_n)|]/(x_i - x_j) \qquad (9)$$

$$\beta(\omega_v) = [\phi(x_i, \omega_n) - \phi(x_j, \omega_n)]/(x_i - x_j) \qquad (10)$$

In the face of the variability of the data, a Least Squares (LSQ) fit to the data was performed. A linear fit was performed to the log magnitude and phase of the data, individually. Also, a complex exponential was LSQ fit to the complex data. The differences were minimal and the following relates to separate fits to the magnitude and phase information as represented in Equations (9) and (10).

The difficulty in performing LSQ fits to the data for the wire above ground arises from two sources: 1) the measurement system had its limitations and beyond a certain spatial point the data could become "noisy" as the noise floor was encountered and 2) contributions to the current other than the transmission line mode could become dominant at sufficiently large distances at high frequencies. Since the branch cut term decays as x^{-2}, it always prevails over the transmission line mode at sufficiently large distances and manifests itself as a flattening of the current magnitude distribution with distance from the source. In fact,

20

modeling of the physical configuration under consideration has confirmed such characteristics. But, the noise floor could provide a similar behavior. Since it does not matter that we identify the structure's cause but only avoid it in our LSQ fits, the initial data fitting involved some "eyeballing" of the data. This required inspection of the log(current magnitude) and of the phase to perform a fit to that part which looked "roughly linear". The danger here is that small errors in the resulting value of attenuation and phase constant could ultimately lead to large errors in the ε_r and σ if the method of solution was not robust.

Examples of the process of evaluating α and β are illustrated in Figures 9 through 12. In Figures 9 and 10 the magnitude and phase data for 30 MHz are shown. Also shown in the Figures 9 and 10 are the linear fits to the log magnitude and phase over the entire range (including all points from 2 through 90), respectively. Figures 11 and 12 show the respective plots for a frequency of 100 MHz. There, the magnitude and phase deviate from linear beyond certain points along the wire. Over the linear portions in both cases one can see the rapidly attenuating slow wave characteristic of the transmission line mode. Of course, when the magnitude begins to decay at a slower rate we may be seeing either the surface attached mode, the branch cut contribution, or evidence of the noise floor. When the phase deviates from linear and slow wave, we begin to see a wave that is increasing in velocity and may eventually reach the velocity in the upper medium or become the fast wave whose existence is predicted theoretically. The orderly behavior of the phase suggests that the cause of the flattened current distribution is not the noise floor but rather the branch cut . Ultimately, however, this issue does not impact our analysis as it is the transmission line mode that provides attenuation and phase constants that are most important in the evaluation of the relative dielectric constant and conductivity.

3.3 Determination of Relative Dielectric Constant and Conductivity

The process of solving for ε_r and σ has already been touched upon. Once values for α and β in the transmission line mode are obtained for a given frequency, the value of $\gamma_p = \beta + i\alpha$ is determined. An iterative solution of the equation $M(\gamma_p) = 0$ for n, the index of refraction for the medium, yields ε_r and σ since $n = (\varepsilon_r + i\sigma/(\omega\varepsilon_0))^{1/2}$. The values of ε_r and σ can range from 1 and 0, respectively, to infinity, although real ground will have a much more limited range. For $\varepsilon_r = 1$ and $\sigma = 0$, the values of α and β will be nearly $\alpha = 0$ and $\beta = k$.
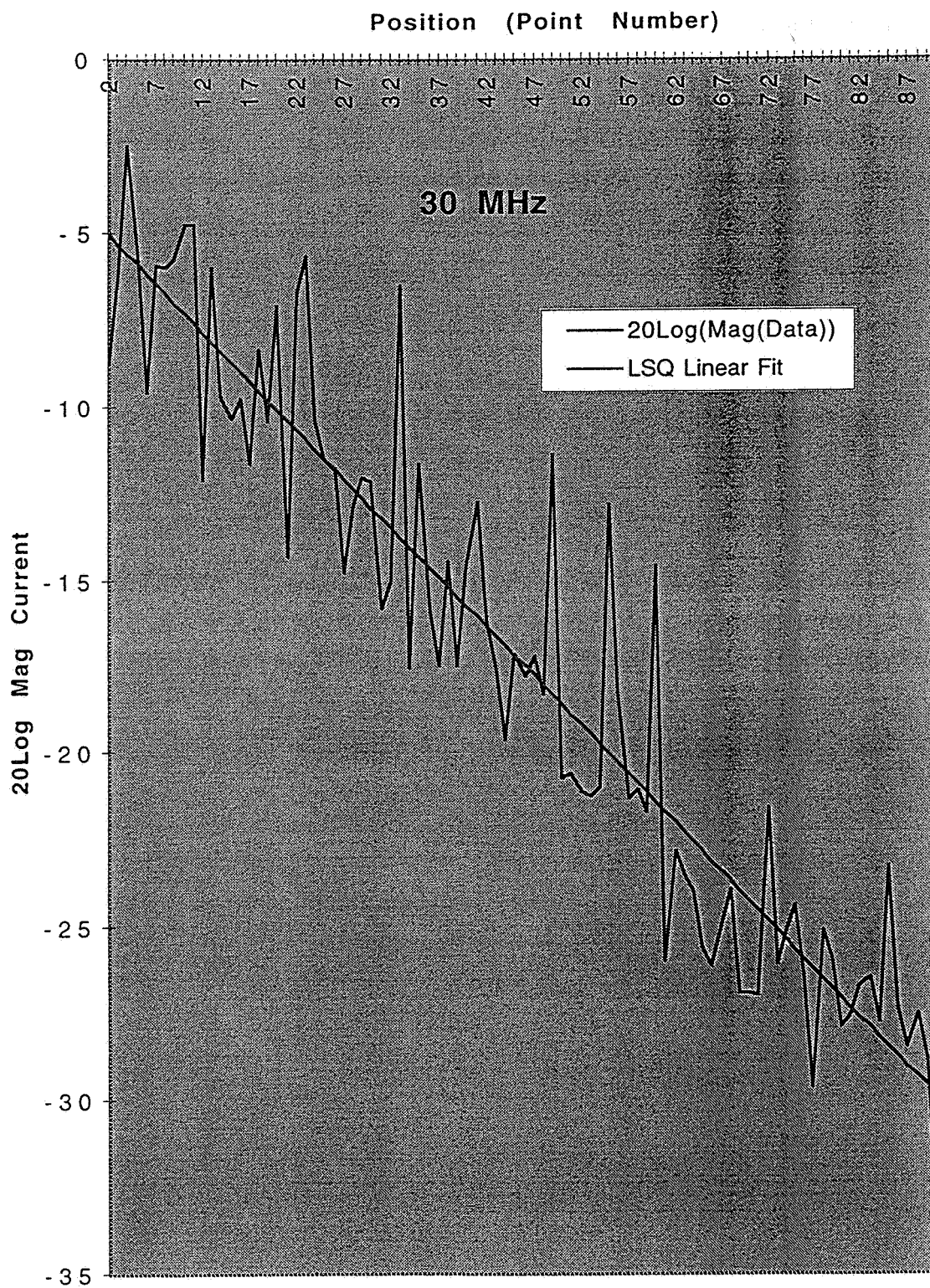
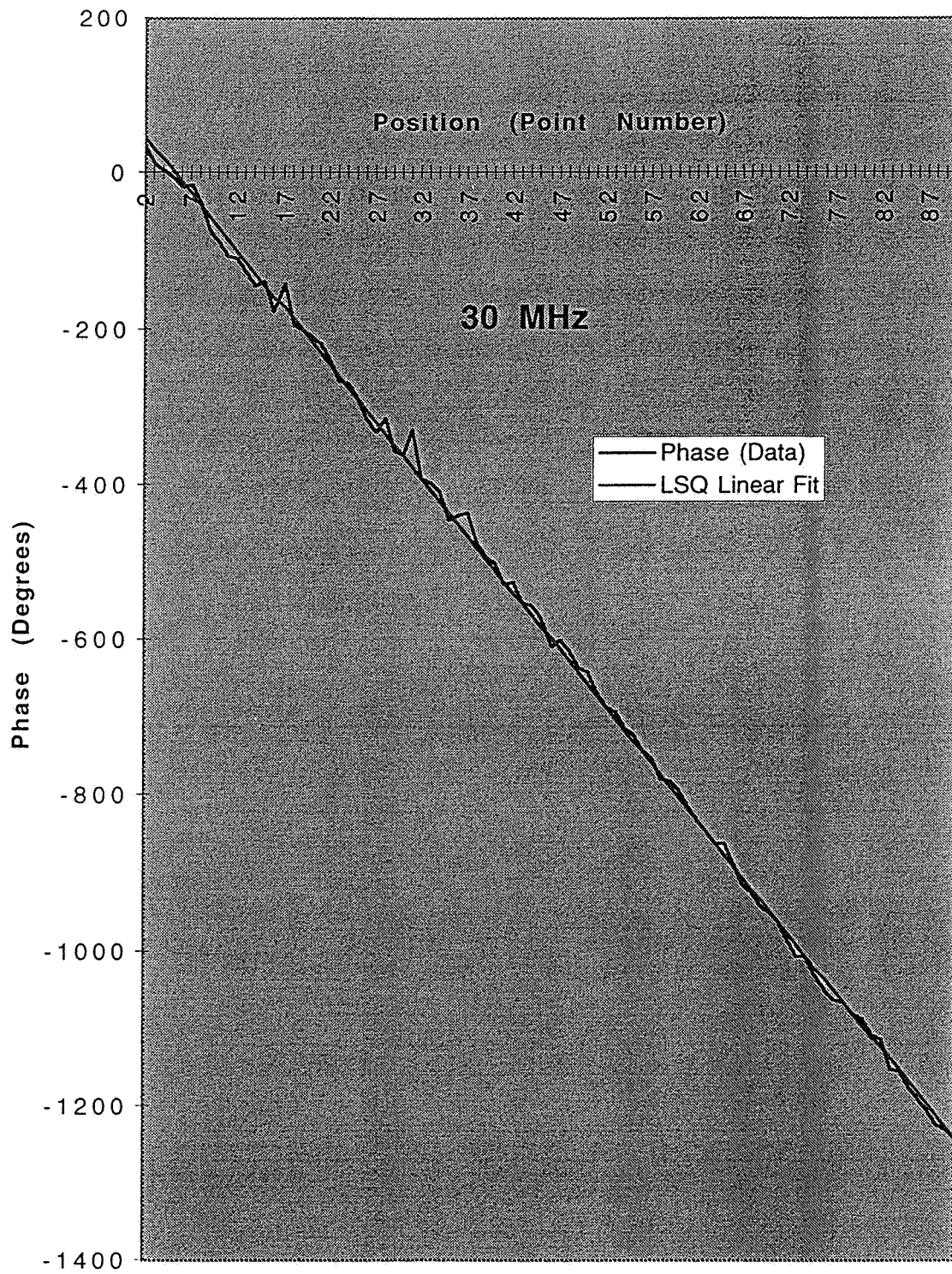Figure 9. Log magnitude of normalized current and linear LSQ fit over Points 2 to 90

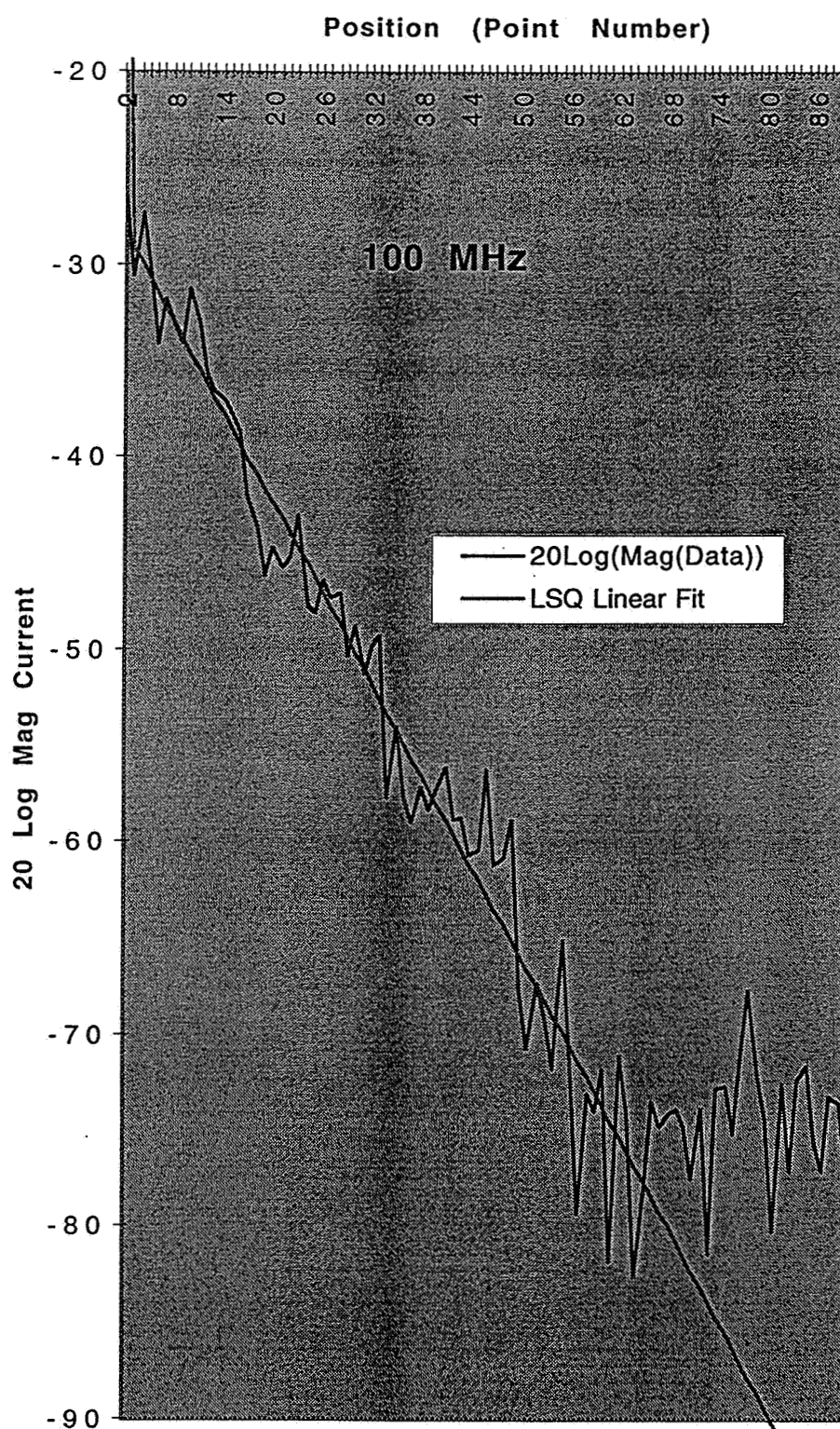Figure 10. Phase of normalized current and linear LSQ fit over Points 2 to 90

23

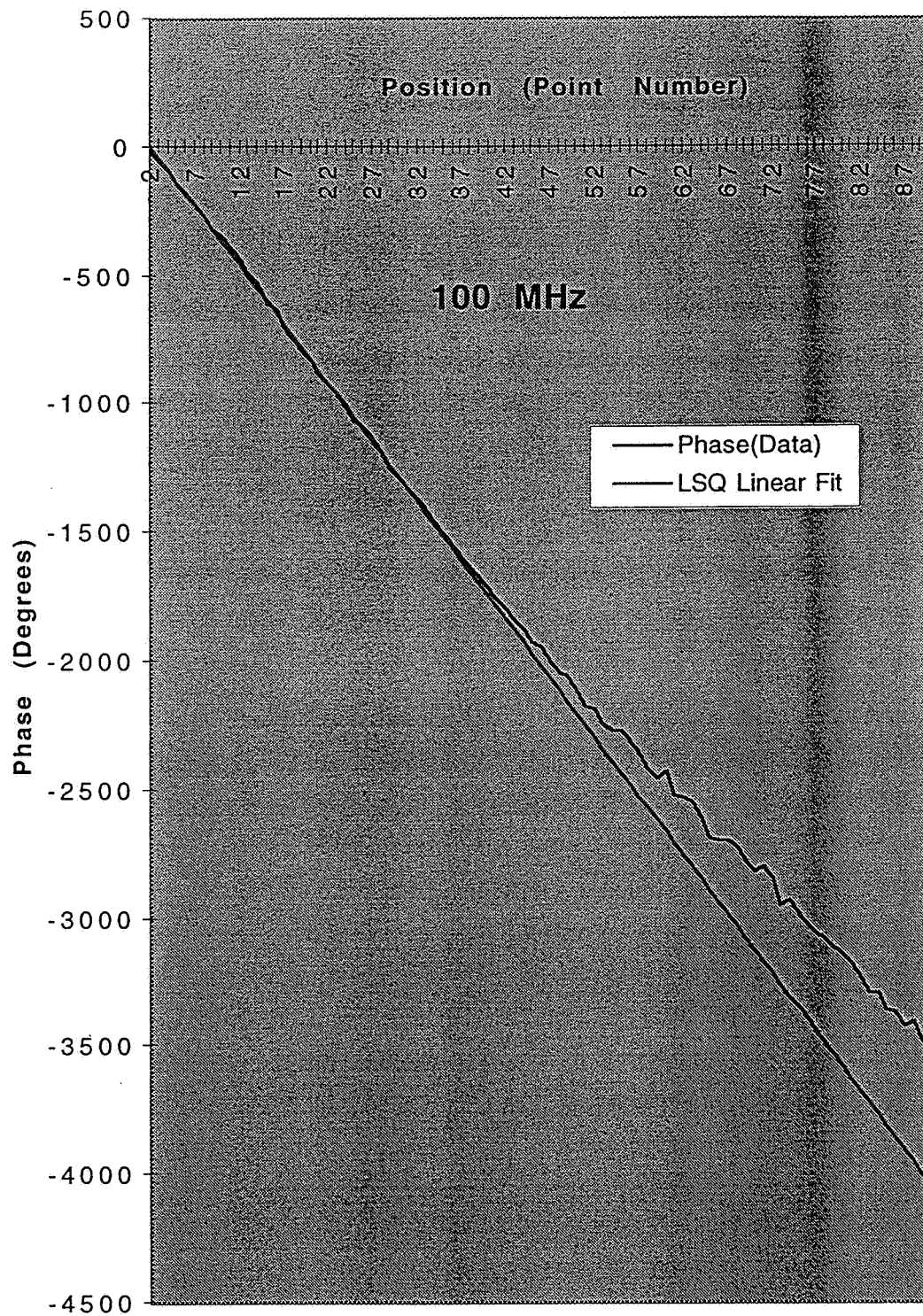Figure 11. Log magnitude of normalized current and linear LSQ fit over Points 2 to 66

24

Figure 12. Phase of normalized current and linear LSQ fit over Points 2 to 30

As ε_r and σ are increased, α and β will both start to increase for the attenuating slow wave of the transmission line mode. However, as ε_r and σ continue to increase α and β will eventually return to nearly $\alpha = 0$ and $\beta = k$, which holds for a wire over perfectly conducting ground. Hence α and β are limited to a range that can only be determined by solving $M(\gamma_p) = 0$ for a given wire height.

A graphical illustration of the process of determining ε_r and σ from α and β is found in Figures 13 and 14. The curves were generated by solving the forward problem (given ε_r and σ, solve $M(\gamma_p) = 0$ for γ_p and therefore for α/k and β/k) with the results plotted as α/k and β/k versus σ with ε_r as a parameter for wire diameter of 3/16 inches and height of 5/8 inches at 10 MHz. An experimentally determined pair α/k and β/k determine horizontal lines on Figures 13 and 14, and values for ε_r and σ representing a solution must fall on these lines in both figures. If no such consistent solution can be found, the cause must be error in the measurement or the experimental parameters. While this graphical approach yields insight into the solution process and its sensitivity to errors, the actual solutions for ε_r and σ were obtained by purely numerical solution of the equation $M(\gamma_p) = 0$.

Since α and β were determined by fitting noisy measured data, and since it was possible that inaccurate values of ε_r and σ could be obtained that were out of the physically possible range, constraints were imposed during the solution process. This increased efficiency and ensured physical realizability of the results. For the cases of interest, the solutions were constrained to lie in a range considered reasonable for concrete materials even with dense rebar inclusions, namely, $1 < \varepsilon_r < 40$ and $0.0001 < \sigma < 0.01$.

The frequency range over which an accurate determination of the attenuation and phase constants was possible was constrained due to several causes. First, the spatial extent over which the current was probed was limited (approximately 26.7 meters) and, at low frequencies, the attenuation in the current was small and difficult to measure accurately. At high frequencies the current decayed quite rapidly so that the linear regions in the log magnitude and phase plots were quite small. In both cases, difficulties were encountered in accurately evaluating attenuation constants and phase factors. In the high frequency case, the LSQ fit was strongly dependent on the chosen range of fit with attendant uncertainties in the constants that were obtained. The behavior seen in Figures 11 and 12 is illustrative of the problem of the shrinking linear region even though, at 100 MHz, it is quite mild. On
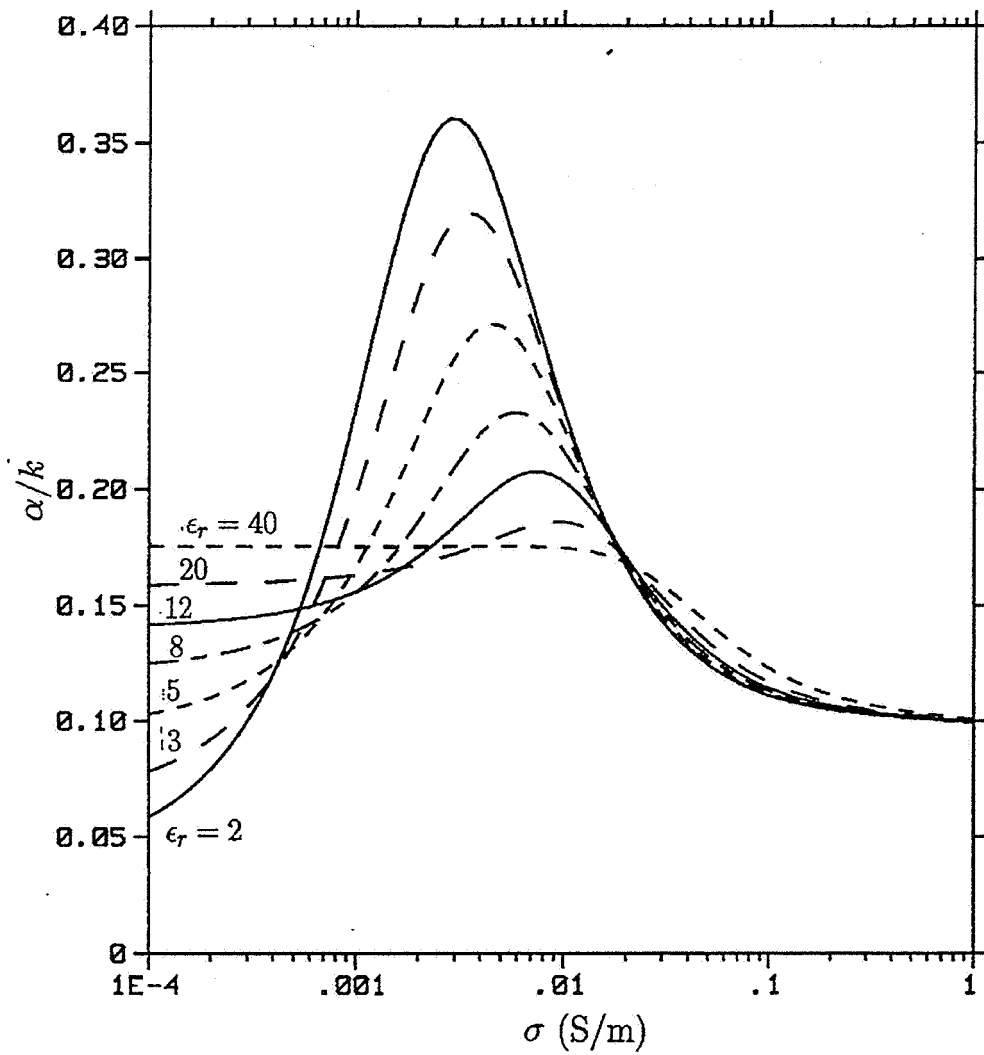
26

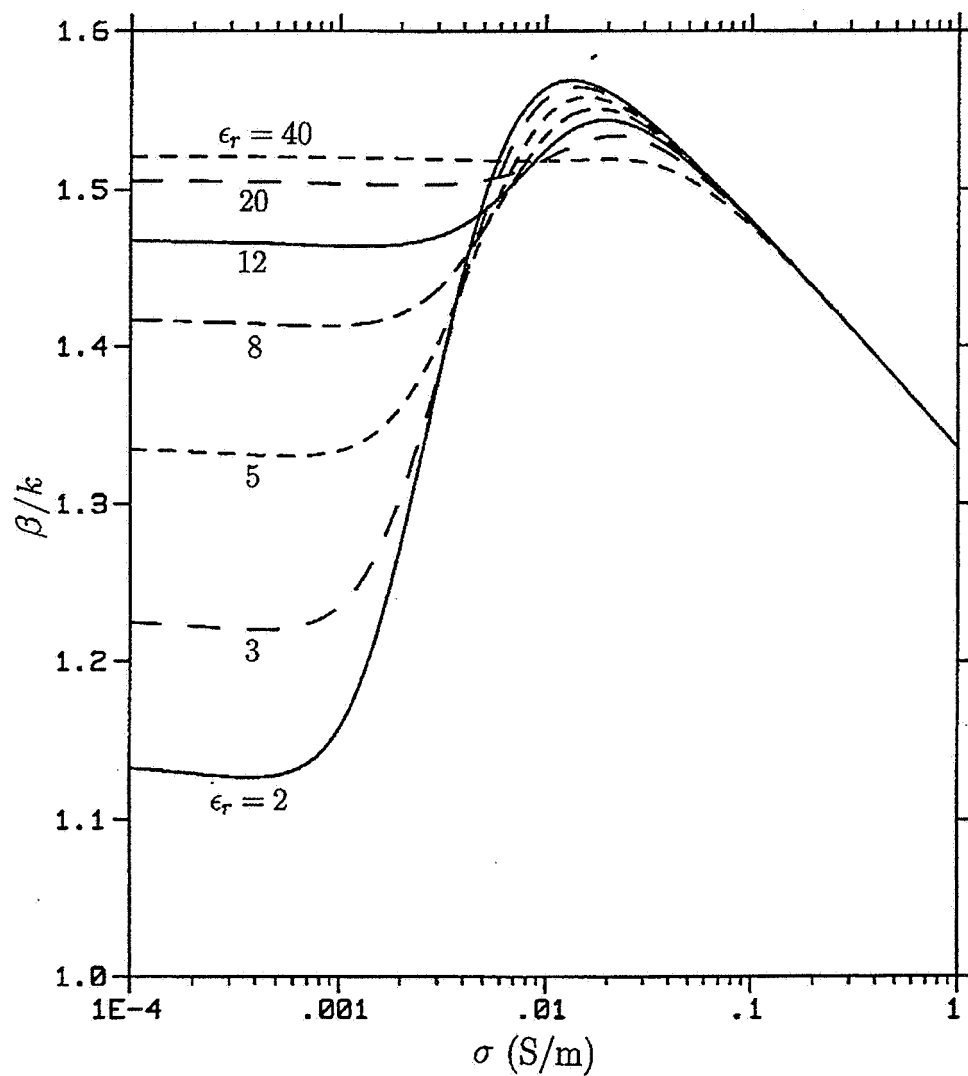Figure 13. Normalized attenuation constant vs. conductivity for various ε_r at 10 MHz

Figure 14. Normalized phase constant vs. conductivity for various ε_r at 10 MHz

the other hand, the behavior of the log magnitude of the current at 250 MHz which is shown in Figure 15 leads to much greater difficulty in defining the linear region and thus leads to greater uncertainty in establishing the value for the attenuation constants. The phase constant determination is also difficult at high frequencies. Figure 16 is the phase plot over 17 points on the wire at 250 MHz. Clearly, the phase change per cell is quite large and errors are possible. Given the available data and the inability to redo portions of the experiment, a range was determined over which the uncertainties in the values for α and β was considered small. For the purposes of our analysis this range was defined as approximately 5 MHz < f < 150 MHz. The lower limit was also consistent with concerns of the experiment personnel regarding their ability to make accurate measurements on the pad in view of previous experience with adverse ground loops and other low frequency limitations. Figure 17 and 18 represent the normalized constants (α/k and β/k) versus frequency as determined from the experimental data.

The data for α and β were used to determine the effective relative dielectric constant and the conductivity of the half space beneath the wire. The process was reasonably robust in the area defined for confidence in estimates of attenuation and phase constants. Outside this range, the process might not return a solution (values of ε and σ were not available which would simultaneously satisfy $M(\gamma_p) = 0$). In some cases, "near" solutions were available in that a given value of ε_r would not yield a unique value of σ but $M(\gamma)$ was almost equal to zero for a range of σ. These data were not used in this analysis.

4. Analysis

In order to extend our estimates for ε_r and σ beyond the range where reliable values of α and β were determined, a theoretical model was used as the underpinning for the results. Such models have been developed in the literature and, for orientational-polarization effects, one has the Debye equations [7,8]

$$\varepsilon_r = \varepsilon_{rinf} + (\varepsilon_{rs} - \varepsilon_{rs}) / (1 + \omega^2\tau^2) \tag{11}$$

$$\sigma = \omega\tau (\varepsilon_{rs} - \varepsilon_{rs}) / (1 + \omega^2\tau^2) \tag{12}$$

where ε_{rinf} is the optical limit for the permittivity, ε_{rs} is the dc value, and τ is the orientational relaxation time for this model. Plots versus frequency of ε_r and σ extracted from the
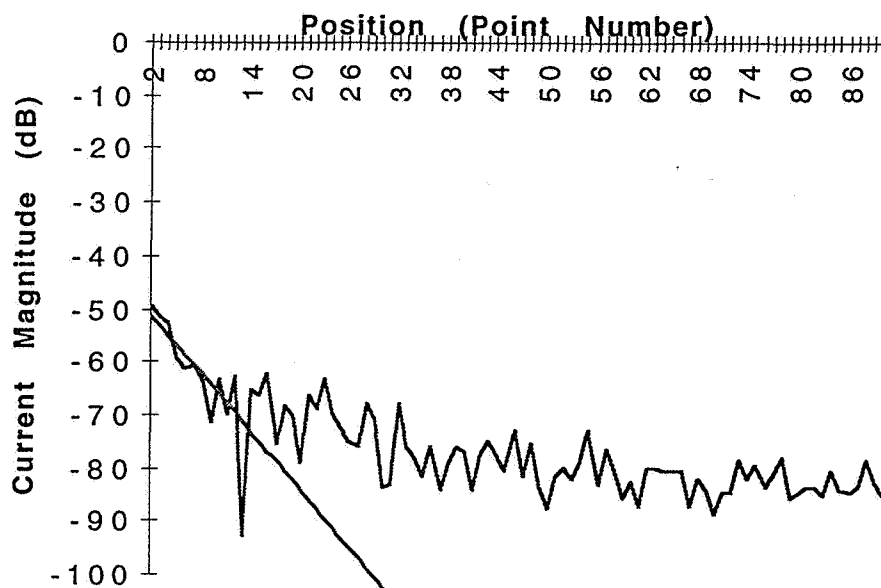
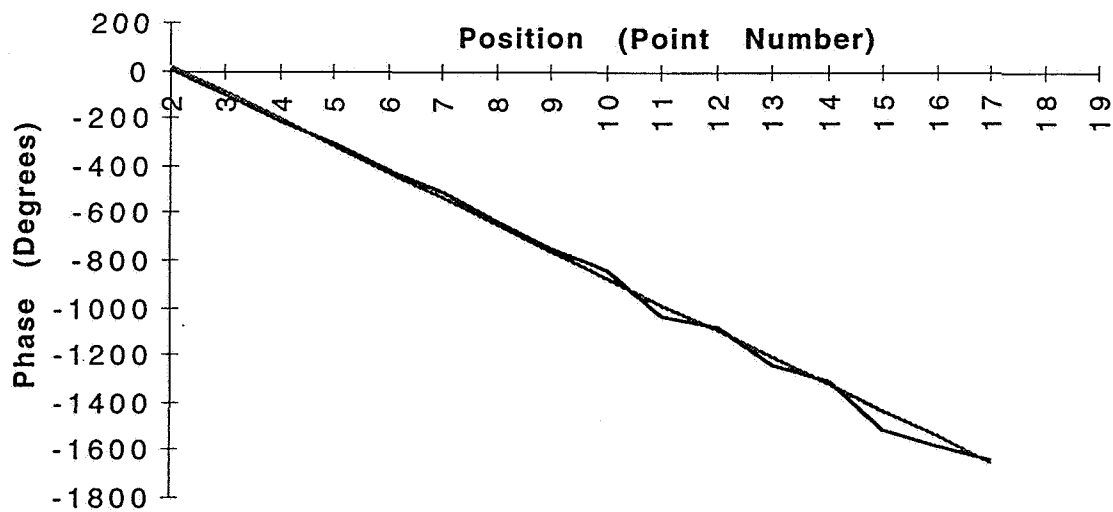Figure 15. Current Magnitude in dB and LSQ fit at 250 MHz

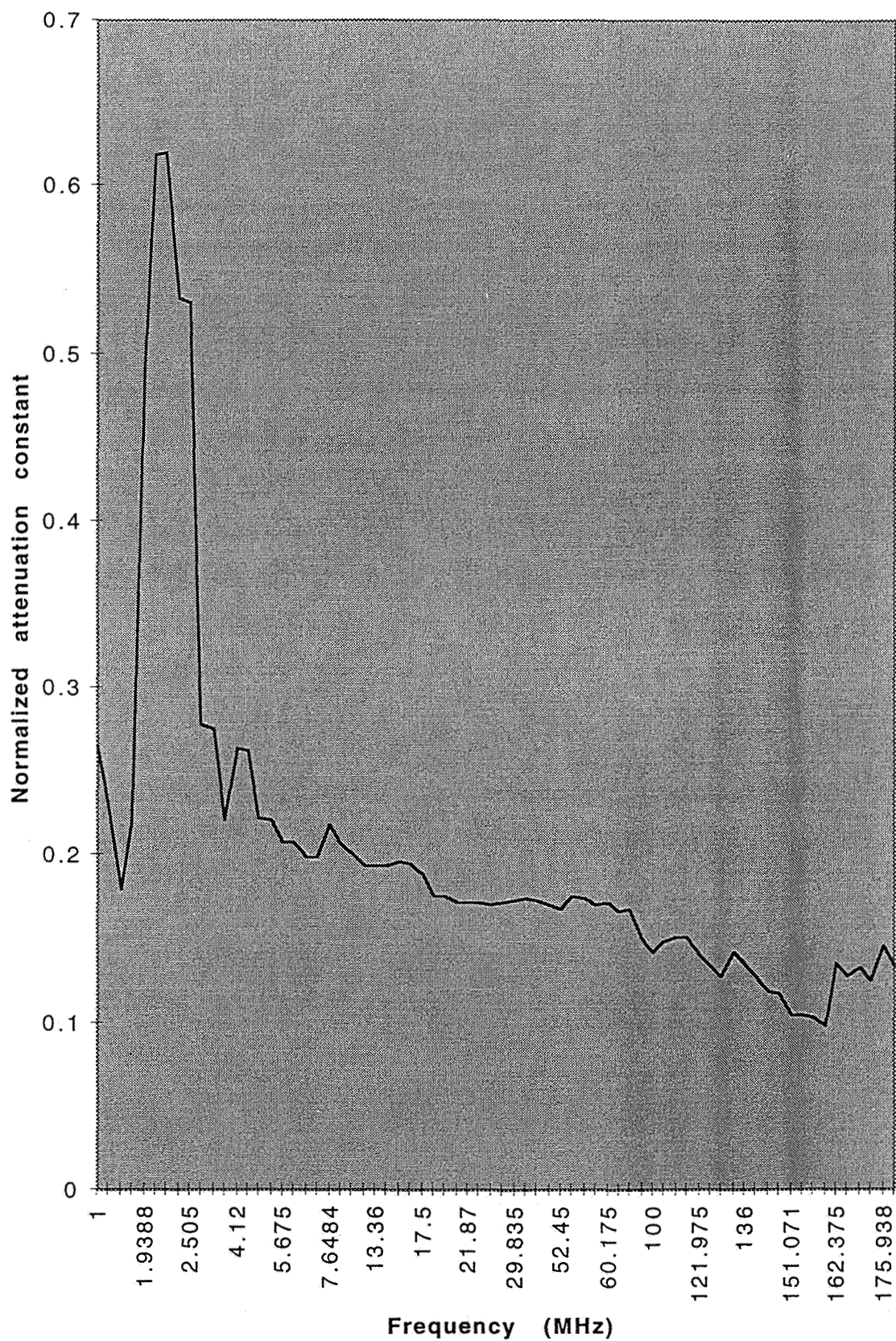Figure 16. Phase of current on wire and LSQ fit over 17 points at 250 MHz

30

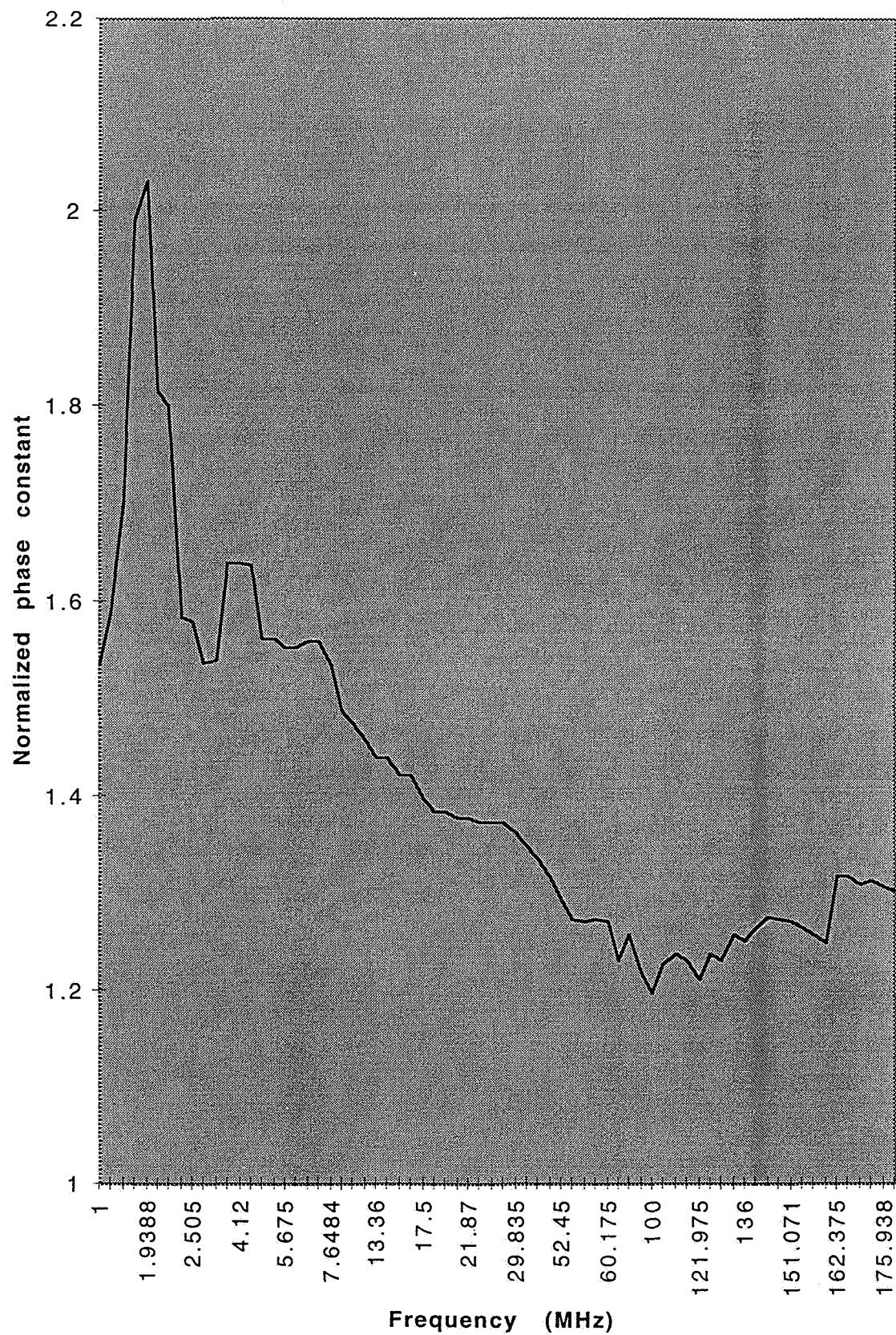Figure 17. Normalized attenuation constant versus frequency

Figure 18. Normalized phase constant versus frequency

32

measured current are shown in Figures 19 and 20, respectively. The anomalous behavior of σ in the range 60 to 80 MHz is not well understood. Also shown in each figure is a least squares fit to the model for the behavior of the constitutive parameters versus frequency. In the LSQ fits performed for the data in hand, the values of ε_{rs}, ε_{rinf} and τ were not the same for the fits of the two sets of data. Clearly, such agreement for the two models would be expected for a perfect model as would ε_r and σ pairs in agreement with the Kronig-Kramers relationships [9]. For the curves shown, however,

$$\varepsilon_r = 4.2418 + 6.1943 / (1 + 1.129 \cdot 10^{-17} \cdot \omega^2) \tag{13}$$

$$\sigma = 4.416 \cdot 10^{-11} \cdot \omega / (1 + 1.354 \cdot 10^{-17} \cdot \omega^2) \text{ for the full range of data} \tag{14}$$

$$\sigma = 3.6385 \cdot 10^{-11} \cdot \omega / (1 + 1.135 \cdot 10^{-17} \cdot \omega^2) \text{ for the restricted data} \tag{15}$$

The restricted data set is composed of the full range of data with frequencies below 18 MHz excluded. The behavior of the permittivity over the frequency range shown is orderly and constrained while that of the conductivity is more variable. Also, the models seem to fit the behavior of the permittivity better than the conductivity. The impact of these issues on propagation in the upper half space is adequately reflected in the variation of the reflection coefficients with variations in the lower medium's wavenumber (or index of refraction, n) which depends on ε_r and σ. This wavenumber arises repeatedly in the analyses and is a key determinant of the reflected and transmitted waves at the interface of the materials when a plane wave, for instance, is incident. The wavenumbers in the pad medium and free space, respectively, are given by

$$k_1 = k_0 n = k_0 [\varepsilon_r (1 + i\sigma/(\omega\varepsilon_0\varepsilon_r)]^{1/2}$$

$$k = k_0 = \omega[\mu_0\varepsilon_0]^{1/2} \tag{16}$$

Two limiting types of propagation in the lower half space are possible, i.e., the conditions under which propagation is conduction or displacement current dominated. Conduction current domination will occur when $\sigma \gg \omega \varepsilon_0 \varepsilon_r$ and will result in a propagation constant that is essentially independent of the relative dielectric constant in the ground, ε_r. On the other hand, displacement current will dominate when $\sigma \ll \omega \varepsilon_0 \varepsilon_r$ and will result in propagation characteristics relatively insensitive to conductivity, σ, and frequency, ω. The "boundary" between these two regions can be said to be approximately

$$\sigma = \omega \varepsilon_0 \varepsilon_r$$

Figure 21 shows such boundaries for frequencies of f = 10, 20, 50, 100, 400, and 1000 MHz. Also shown in the figure is a contour connecting elements of the set of $\{\varepsilon,\sigma\}$ pairs that have been determined experimentally. The sequencing, which is in ascending values
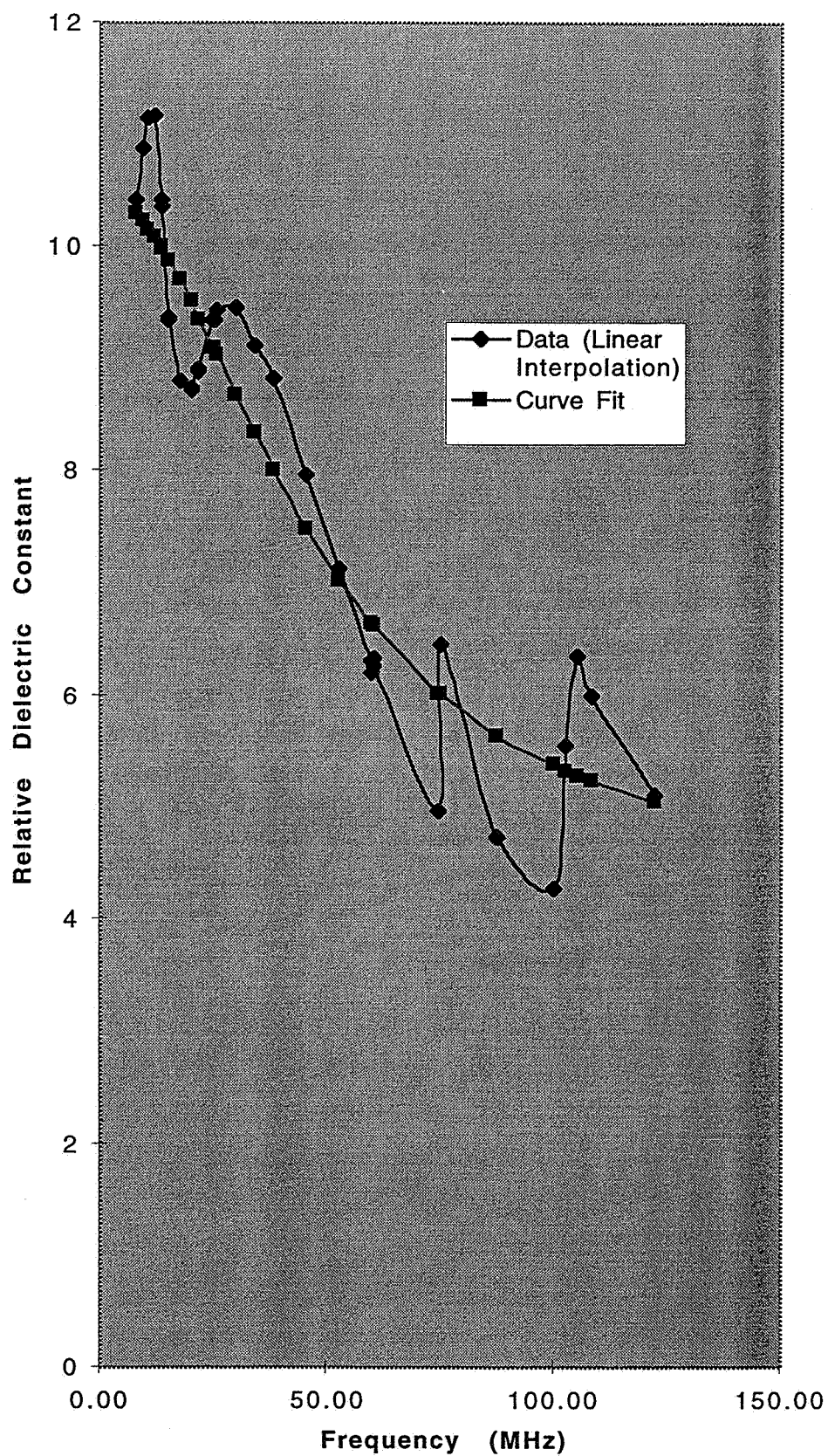
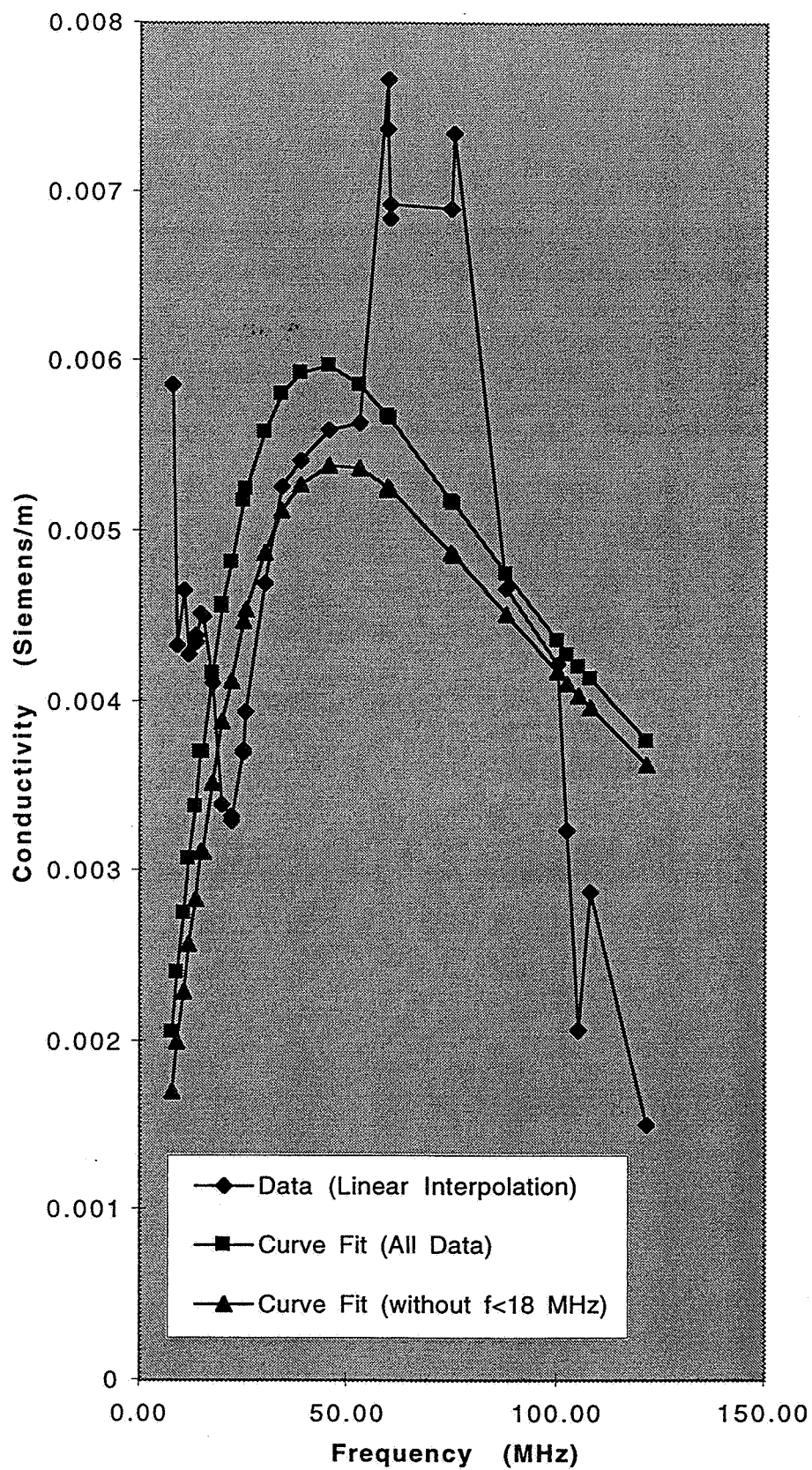Figure 19. Relative dielectric constant versus frequency - experimental data and curve fit

34

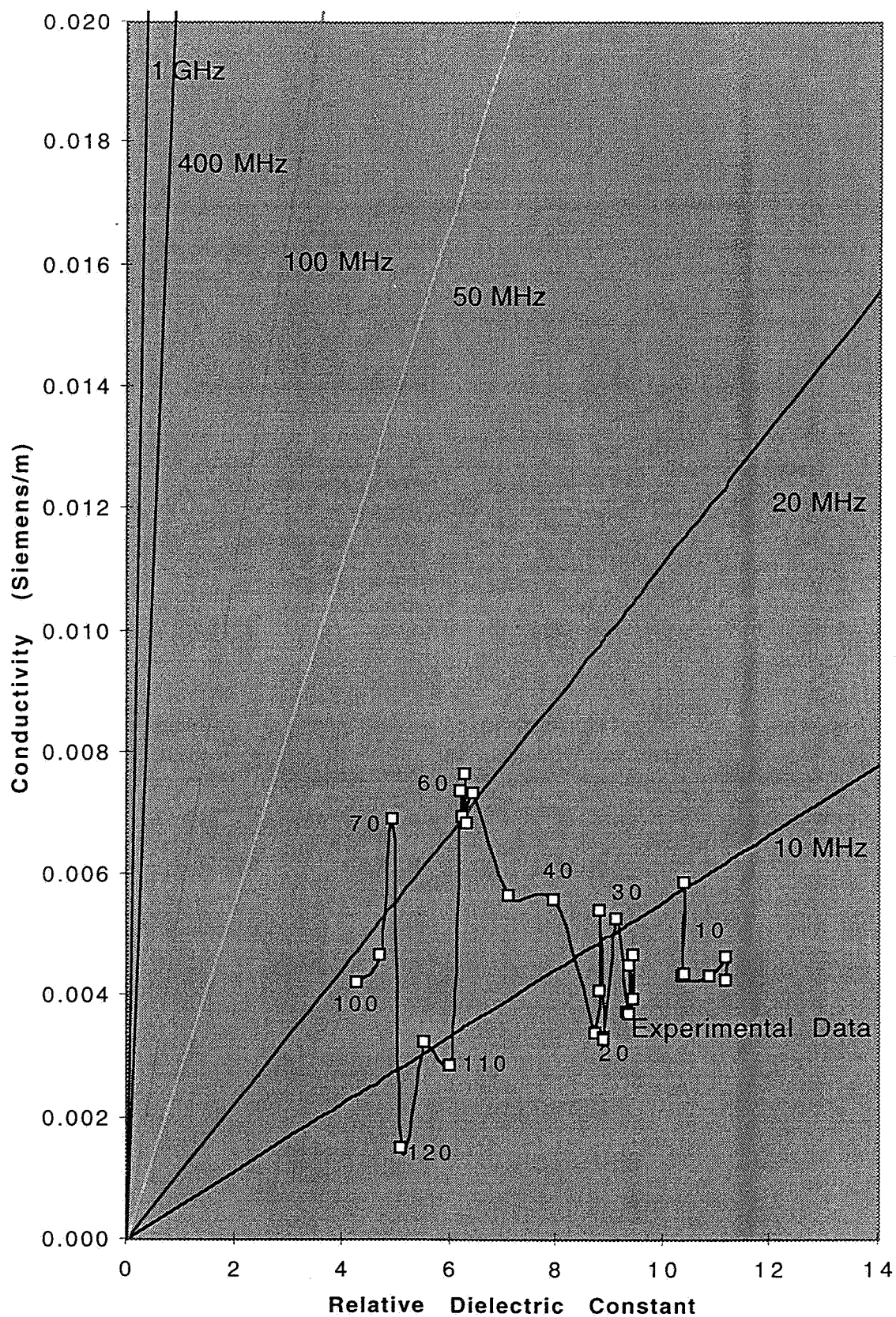Figure 20. Conductivity versus frequency - experimental data and curve fits

Figure 21. Displacement/Conduction boundaries and experimental $\{\varepsilon_r, \sigma\}$ with frequencies

of conductivity, does not convey any physical information. The important feature to be observed in the figure is the range of the $\{\varepsilon,\sigma\}$ set and the fact that the propagation is displacement current dominated at frequencies above about 20 to 50 MHz. Another feature is that for the material under study, using average values over the frequency range (f_1,f_2) of Equations (13) and (14),

$$< \varepsilon_r(f_1,f_2) > = 4.24 + 2.93 \bullet 10^8 \bullet [\tan^{-1}(2.11 \bullet 10^8 \bullet f_2) - \tan^{-1}(2.11 \bullet 10^8 \bullet f_1)] / (f_2 - f_1)$$

$$< \sigma(f_1,f_2) > = 2.595 \bullet 10^5 \bullet \ln[(1 + 5.29 \bullet 10^{-16} \bullet f_2^2) / (1 + 5.29 \bullet 10^{-16} \bullet f_1^2)] / (f_2 - f_1)$$

one finds that average values of $\varepsilon_r \sim 7$ and $\sigma \sim 0.005$ appear to be reasonable over the 10 to 100 MHz range. Of course, for frequencies above 50 MHz the values of the conductivity may be of secondary importance.

To further support the observations based on the behavior of the propagation constant or wavenumber in the pad material, attention was directed towards the Fresnel reflection coefficients at the pad interface. These reflection coefficients are given by

$$R_H = [\mu_1 k_0 \cos\theta - \mu_0(k_1^2 - k_0^2 \sin^2\theta)^{1/2}] / [\mu_1 k_0 \cos\theta + \mu_0(k_1^2 - k_0^2 \sin^2\theta)^{1/2}] \qquad (17)$$

$$R_E = [\mu_0 k_1^2 \cos\theta - \mu_1 k_0(k_1^2 - k_0^2 \sin^2\theta)^{1/2}] / [\mu_0 k_1^2 \cos\theta + \mu_1 k_0(k_1^2 - k_0^2 \sin^2\theta)^{1/2}] \qquad (18)$$

with θ measured from the normal to the surface, the subscript E denoting the electric field vector in the plane of incidence, subscript H denoting the electric field vector perpendicular to the plane of incidence, and the subscript 1 denoting the subsurface material (concrete, steel, soil, etc.). Figures 22 to 26 are contour plots of the reflection coefficient magnitude in $\varepsilon_r - \sigma$ space for select frequencies in the range of interest. The values of the contours (magnitude of R) are not as important and are not shown. Rather, the curves are meant to convey that the reflection coefficients (both R_E and R_H) for the range of incidence angles are mainly functions of ε_R and are therefore displacement current dominated. The implication is that for frequencies greater than about 32 MHz (or thereabouts), the precise definition of σ is not as important as an accurate definition of ε_R.

The expressions used in the LSQ fits (Equations (13) and (14)) were plotted parametrically over the range of 0 MHz to 1 GHz. A version of Figure 21 with the LSQ-fit curve is shown in Figure 27. The fit is reasonable for the purposes of understanding the impact of $\{\varepsilon_r,\sigma\}$. Clearly, the constitutive parameter values lead to strong displacement current
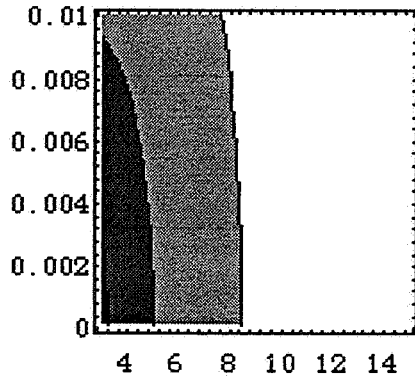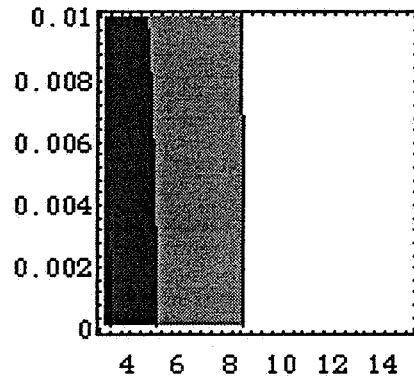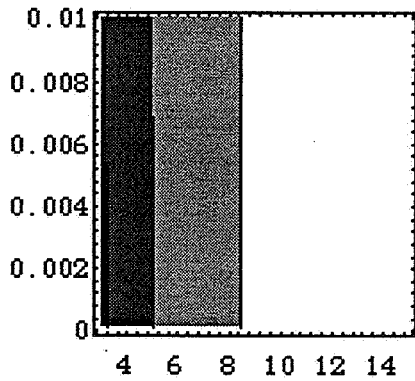
16 MHz
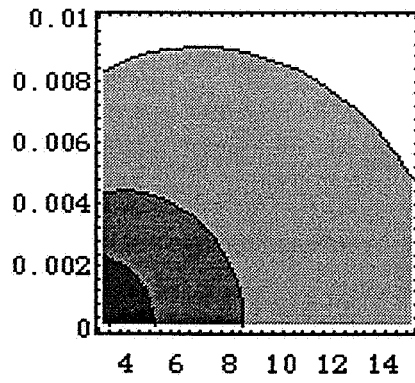
32 MHz
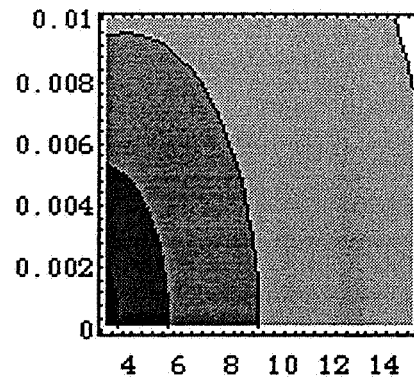
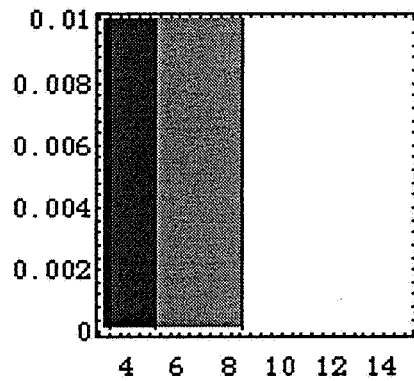64 MHz

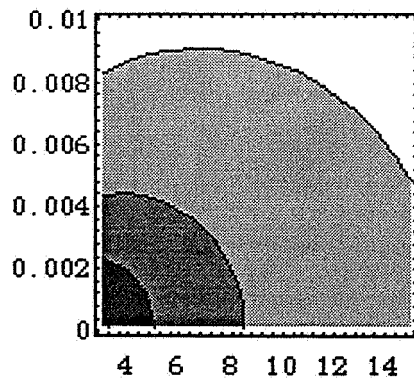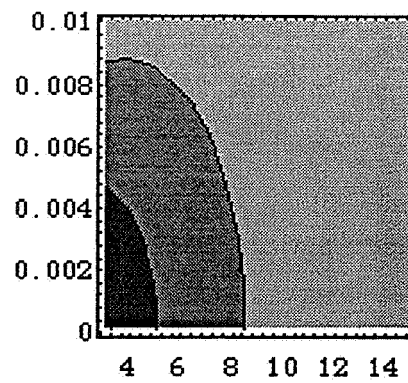128 MHz

256 MHz

512 MHz

Figure 22. $R_E = R_H$ for normal incidence ($\theta = 0$) (Vertical axes are conductivity in Siemens/m and horizontal axes are relative dielectric constant)

16 MHz

32 MHz

64 MHz
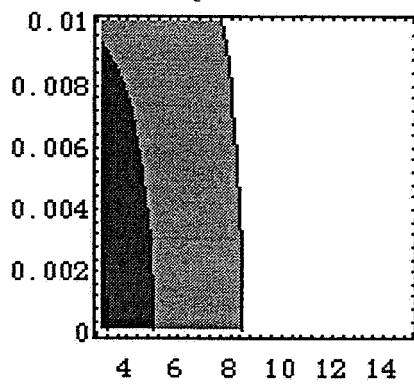
128 MHz
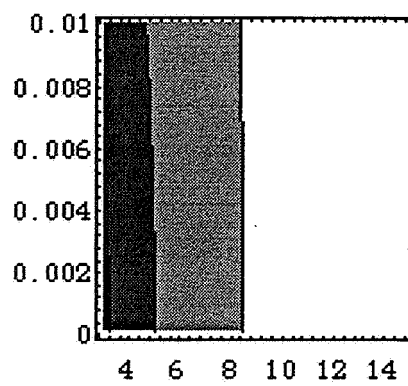
256 MHz
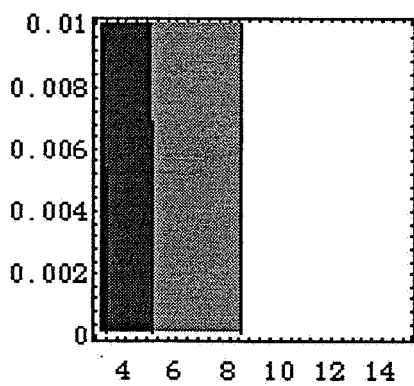
512 MHz
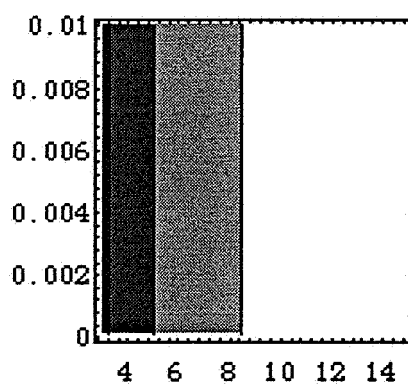
Figure 23. R_H for incidence at 45 degrees (Vertical axes are conductivity in Siemens/m and horizontal axes are relative dielectric constant)

16 MHz

32 MHz

64 MHz

128 MHz

256 MHz

512 MHz

Figure 24. R_E for incidence at 45 degrees (Vertical axes are conductivity in Siemens/m and horizontal axes are relative dielectric constant)

16 MHz

32 MHz

64 MHz

128 MHz

256 MHz

512 MHz

Figure 25. R_H for grazing angle of incidence (85 degrees from normal incidence) (Vertical axes are conductivity in Siemens/m and horizontal axes are relative dielectric constant)

Figure 26. R_E for grazing angle of incidence (85 degrees from normal incidence) (Vertical axes are conductivity in Siemens/m and horizontal axes are relative dielectric constant)

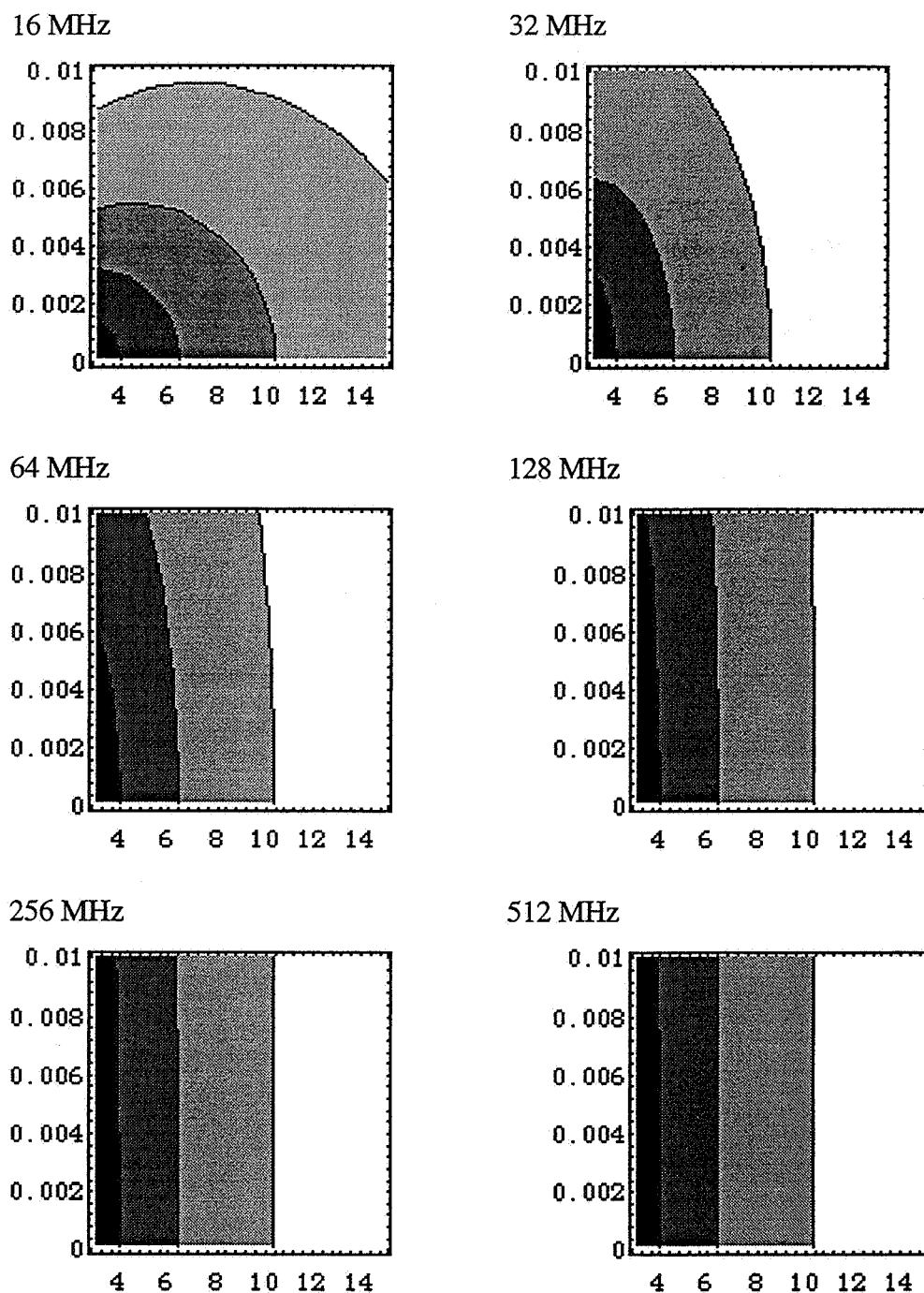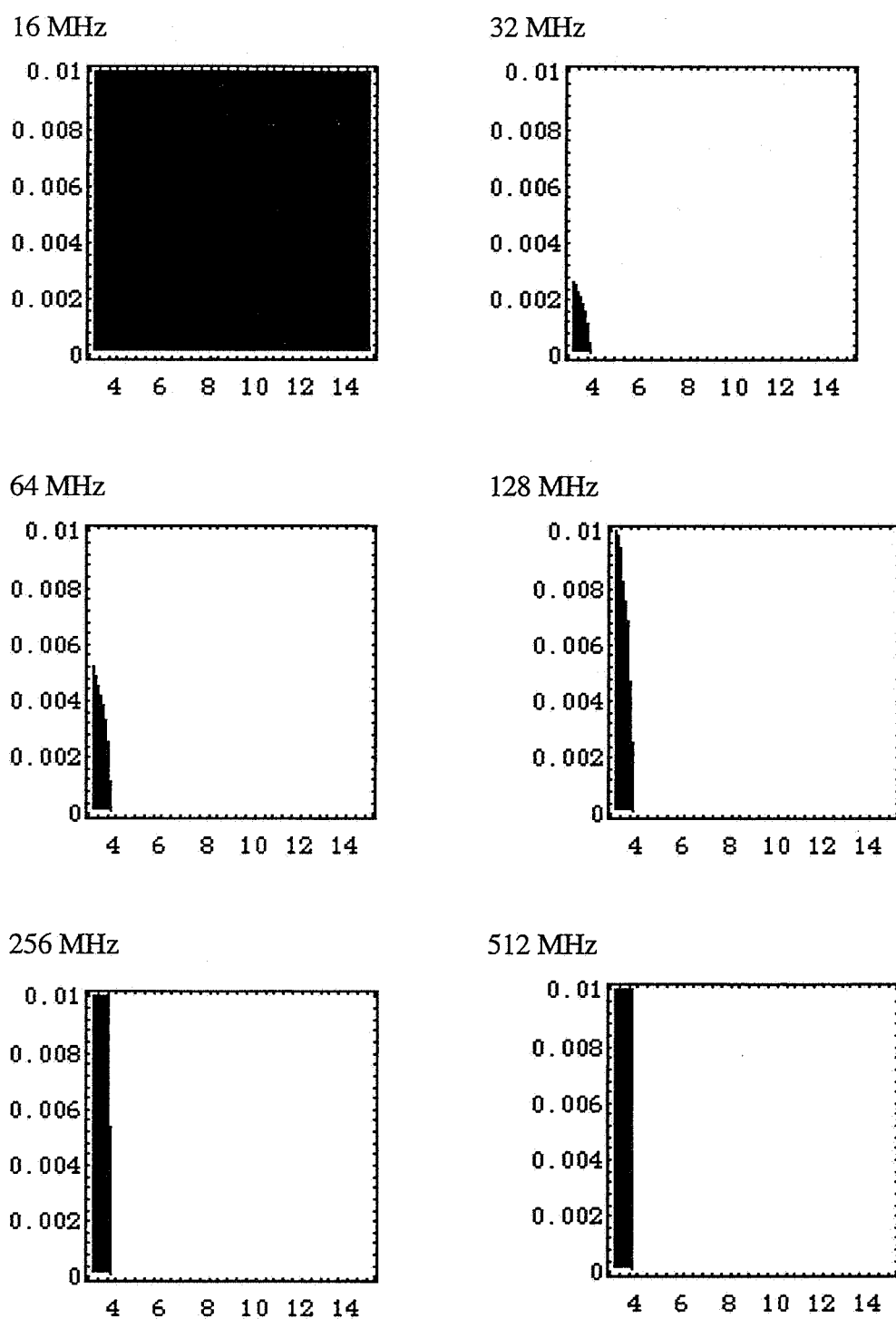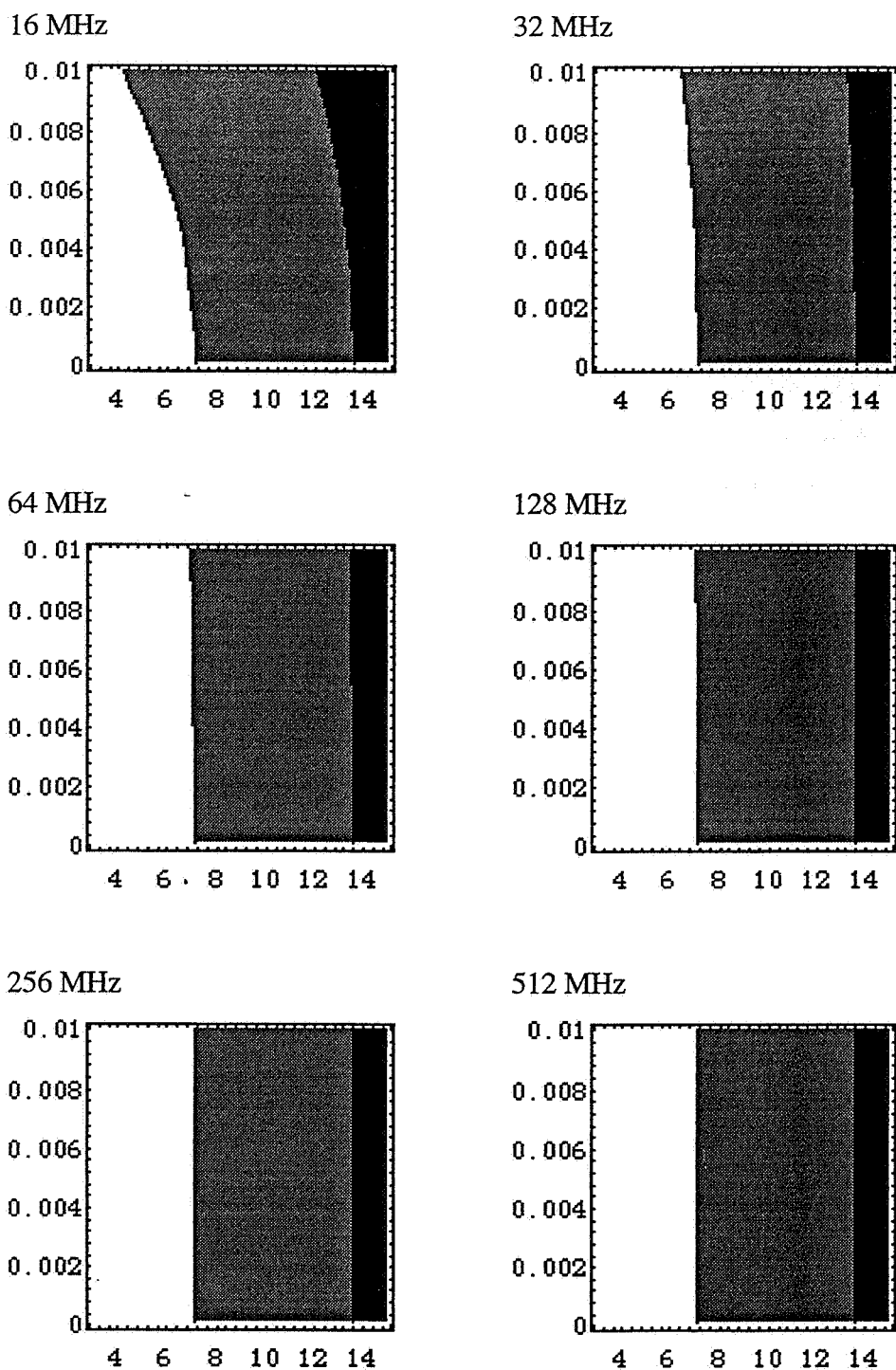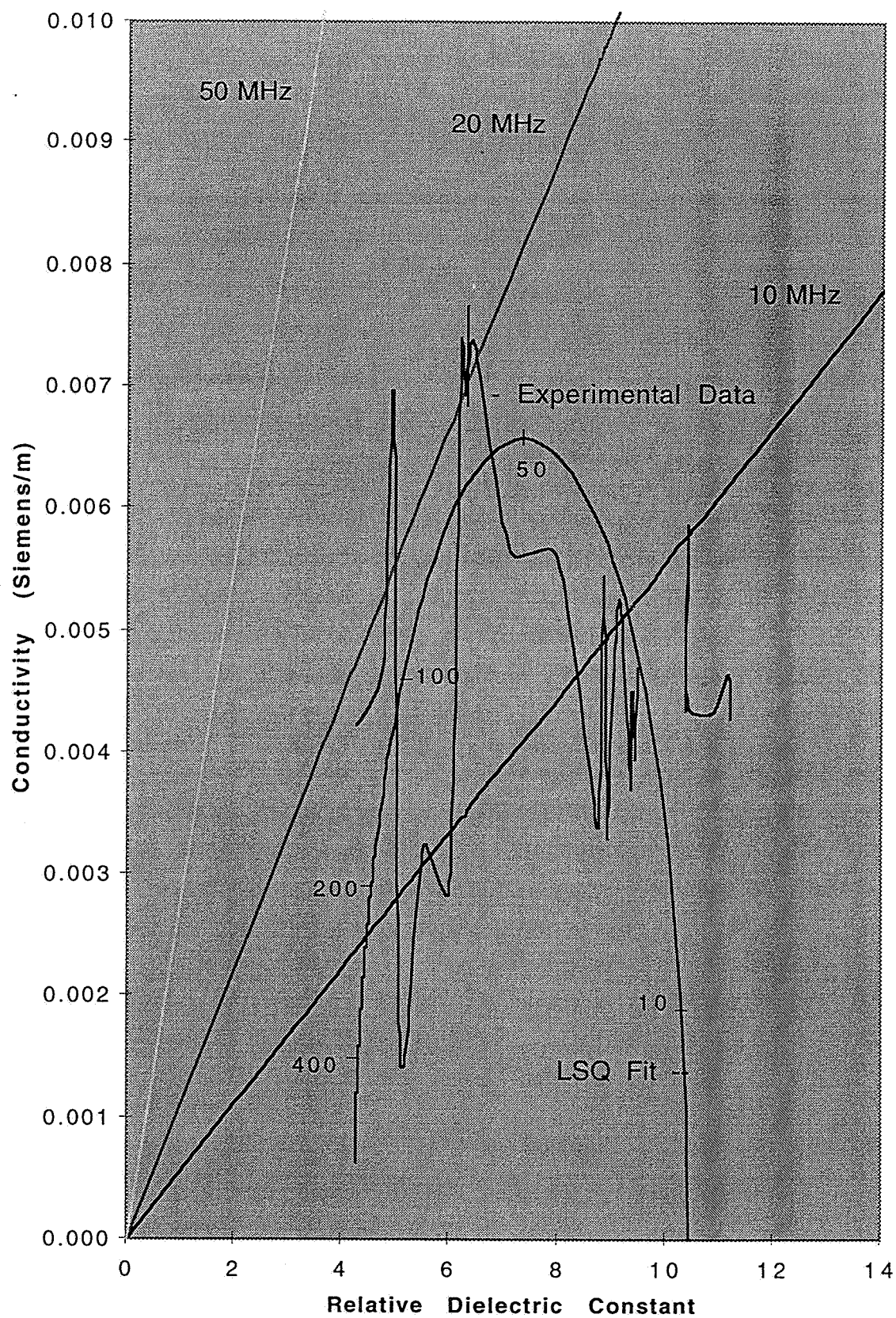Figure 27. Experimental data and LSQ fit for the constitutive parameters

effects and the system is generally displacement current dominated. Plots of the relative dielectric constant and conductivity are shown in Figures 28 and 29 for frequencies up to about 300 MHz to illustrate that the region of variability of the parameters is rather confined.

Another indicator of the importance of conduction or displacement current effects is the index of refraction for the medium, i.e.,

$$n = [\varepsilon_r + i\sigma/(\omega e_0)]^{1/2} \tag{19}$$

Clearly, σ becomes unimportant when n can be adequately represented by

$$n \sim [\varepsilon_r]^{1/2} \tag{20}$$

Figure 30 shows curves representing the magnitude of Equations (19) and (20) and illustrates that above about 40 MHz, the differences are less than 3%. Above about 150 MHz, the index of refraction has effectively lost its dependence on frequency, and above 100 MHz, it has lost its strong dependency on σ. The index of refraction is, however, strongly affected by the values used for the relative dielectric constant throughout the entire frequency range.

Finally, the magnitude of the reflection coefficient was considered as a measure of the importance of σ. For our purposes, only the normal incidence coefficient was evaluated using the index of refraction in Equation (19) and the approximation ($\sigma = 0$) given by Equation (20). Figure 31 is a plot of the two representations for $R_E = R_H$ for normal incidence. The deviation in the magnitude is less than about 5% for all frequencies. The reflection coefficient is effectively independent of frequency above 150 MHz and nearly so above 80 MHz. It is nearly independent of σ above 50 MHz.

The previous discussions have considered only the relative importance of ε_r and σ in the determination of parameters defining wave propagation in the medium. In the following we consider the magnitude of the index of refraction evaluated from the constitutive parameters resulting from our measurements, and look at its comparison to the magnitude of the index obtained from our models for the constitutive parameters based on LSQ fits to our data. Figure 32 is a plot of the magnitude of n versus frequency using the model for ε_r and σ as compared to the magnitude as determined from ε_r and σ obtained from processing

44

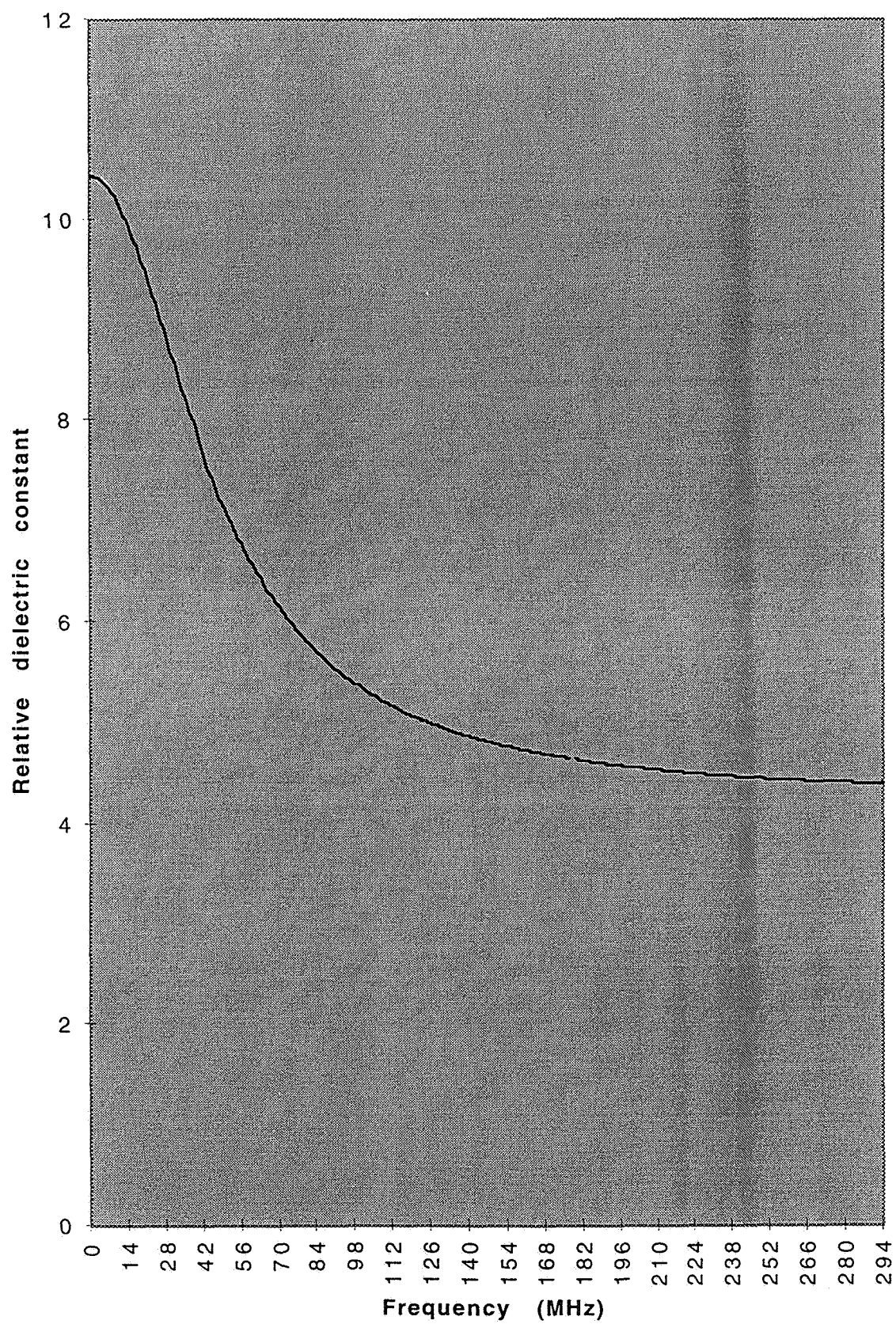Figure 28. Relative dielectric constant versus frequency per Equation (13)
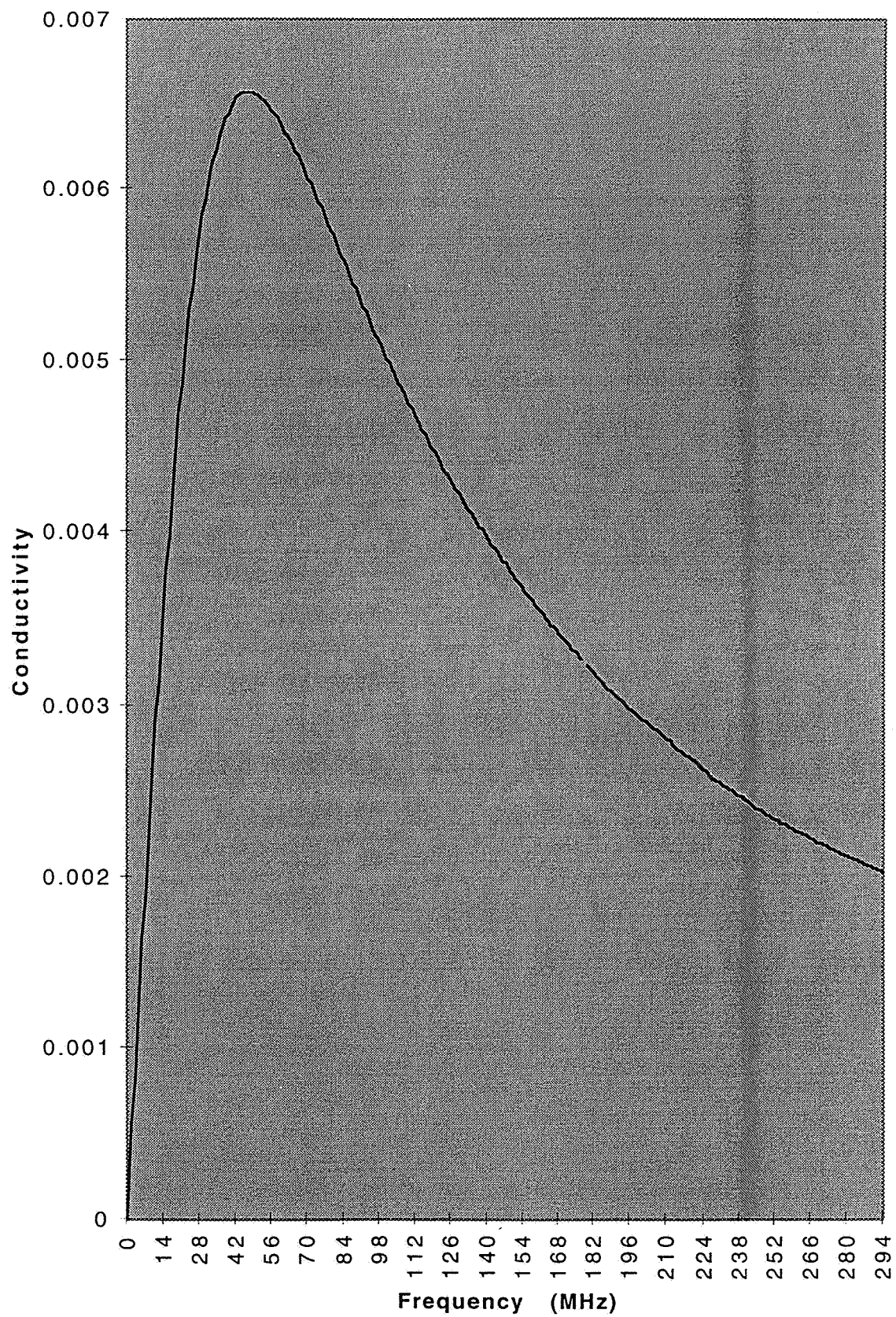
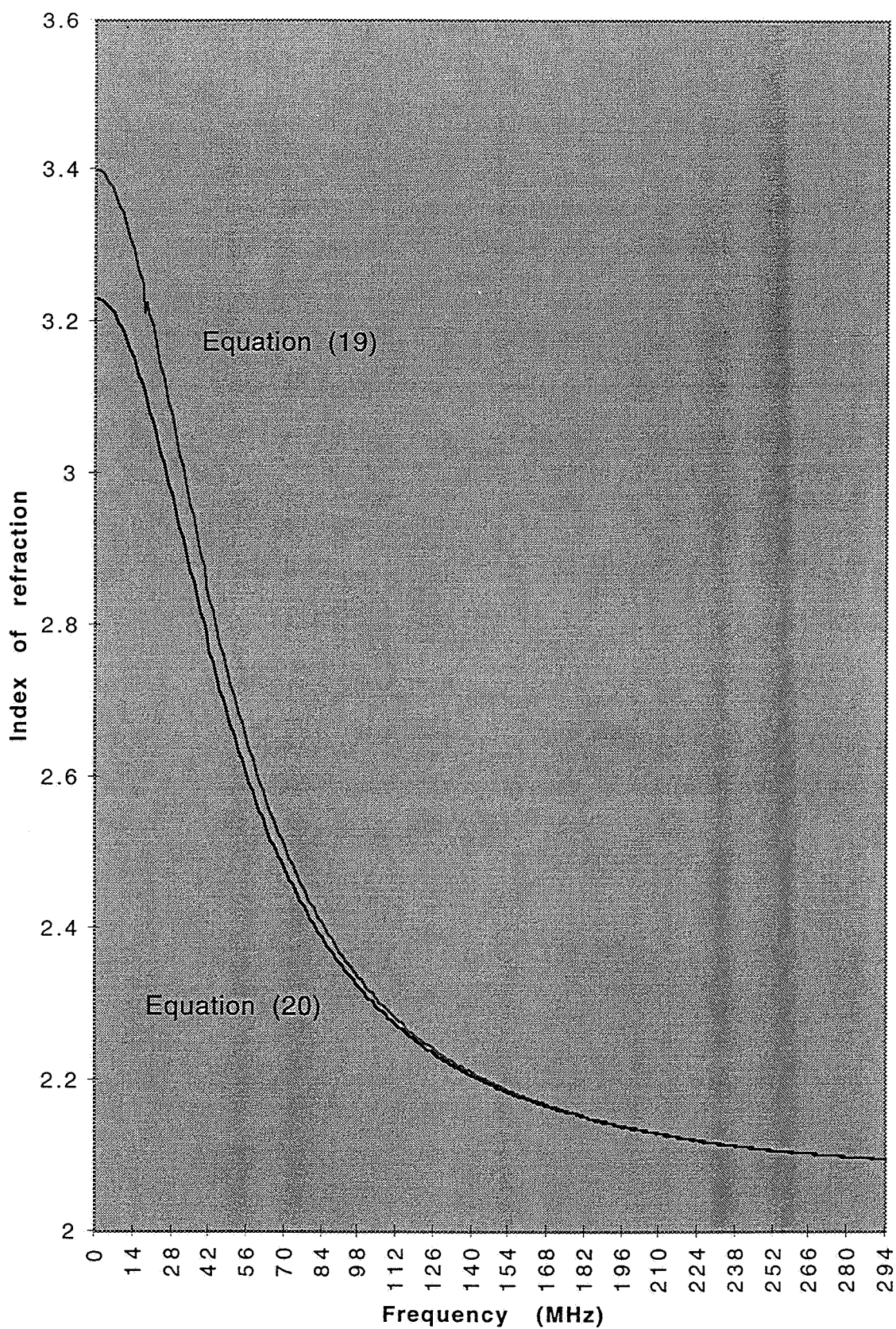Figure 29. Conductivity (Siemens/m) versus frequency per Equation (14)

Figure 30. Two representations for the index of refraction versus frequency
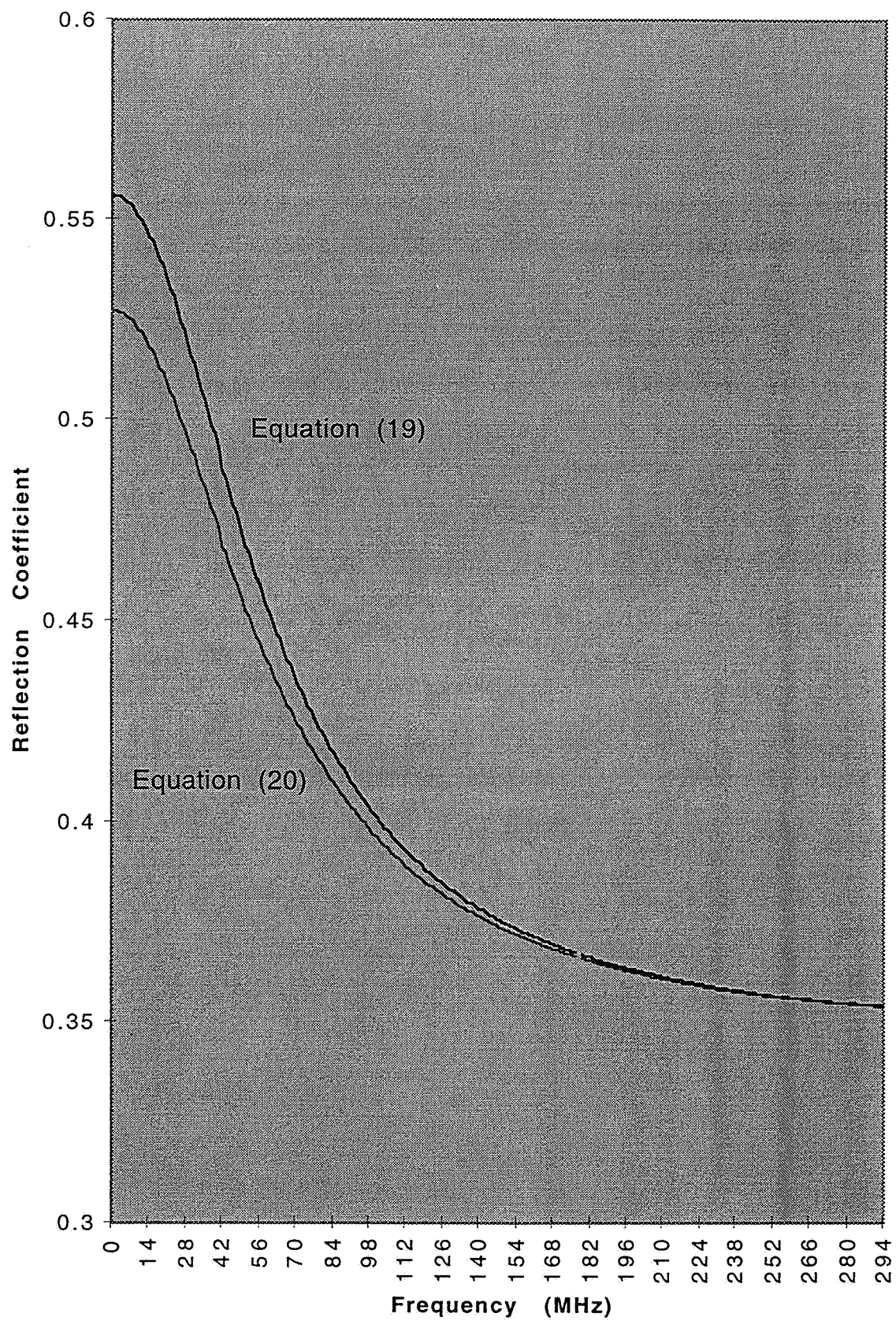
Figure 31. Two representations for the normal incidence reflection coefficient vs. frequency
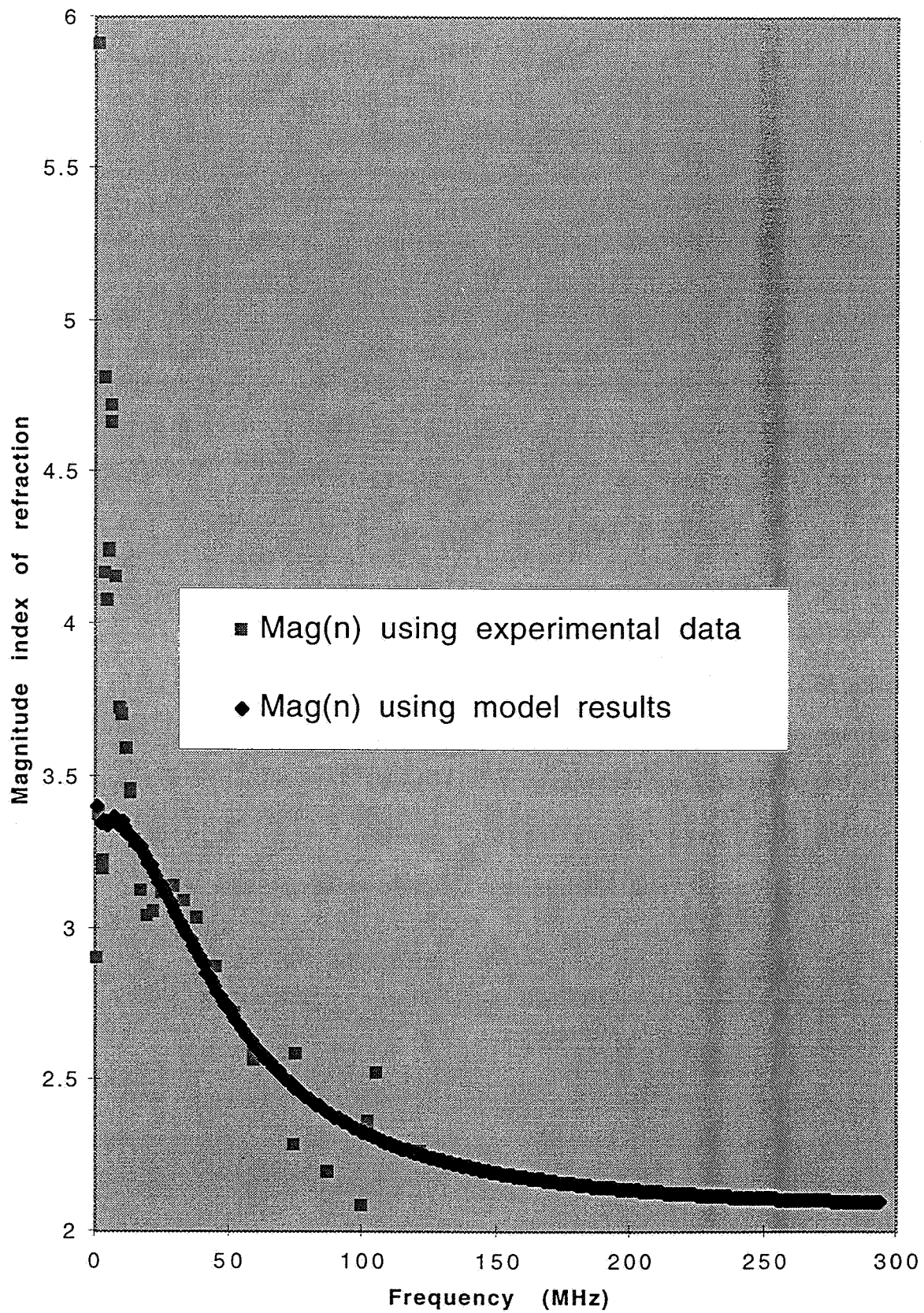
48

Figure 32. Magnitude of index of refraction as obtained from raw data and from models

our experimental data. The agreement over the range from 18 MHz or so through 126 MHz is quite reasonable and provides some confidence in using the models for prediction at higher frequencies. The apparent discrepancy between the model and the experimentally-based results may be in part due to the difficulty in determining α and β, and ultimately ε_r and σ, from the experimental data.

The relative sensitivity of the reflection coefficient to variations in the index of refraction for the special condition where $\mu_1 = \mu_0$ will be considered to provide some indication of the effects of errors in the process. A full error analysis is beyond the scope of this report. With

$$R_H = [\cos\theta - (n^2 - \sin^2\theta)^{1/2}] \, / \, [\cos\theta + (n^2 - \sin^2\theta)^{1/2}] \qquad (21)$$

$$R_E = [n^2\cos\theta - (n^2 - \sin^2\theta)^{1/2}] \, / \, [n^2\cos\theta + (n^2 - \sin^2\theta)^{1/2}] \qquad (22)$$

consideration will be given to

$$(1 \, / \, R_H) \, (\partial R_H \, / \, \partial n) = 2 \, n \cos\theta \, (n^2 - 1)^{-1} (n^2 - \sin^2\theta)^{-1/2} \qquad (23)$$

$$(1 \, / \, R_E) \, (\partial R_E \, / \, \partial n) = 2 \, n \cos\theta \, (n^2 - \sin^2\theta)^{-1/2} (n^2 - 2 \sin^2\theta) \, / \, (n^4\cos^2\theta - n^2 + \sin^2\theta) \qquad (24)$$

An approximation for the fractional change due to changes in n is

$$| \, \Delta R_H \, / \, R_H \, | = 2 \, | \, n \cos\theta \, (n^2 - 1)^{-1} \, (n^2 - \sin^2\theta)^{-1/2} \, \Delta n \, | \qquad (25)$$

$$| \, \Delta R_E \, / \, R_E \, | = 2 \, | \, n \cos\theta \, (n^2 - \sin^2\theta)^{-1/2} \, (n^2 - 2 \sin^2\theta) \, / \, (n^4\cos^2\theta - n^2 + \sin^2\theta) \, \Delta n \, | \qquad (26)$$

Over the range from 20 to 120 MHz (the range of the experimental data in Figure 32), we find that $| \, \Delta R_H \, / \, R_H \, | \leq 0.6 \, | \, \Delta n \, |$ and $| \, \Delta R_E \, / \, R_E \, | \leq 1.5 \, | \, \Delta n \, |$. The maximum value in the latter result is an overestimated bound except in the vicinity of the Brewster angle. Removed from the Brewster angle, the result for R_E is in keeping with the result for R_H.

In view of the observations made in this section, the constitutive parameters determined from experimental data over a limited frequency range and the models based on these limited data appear to yield reliable values outside the range of the useable experimental data.

50

5. Conclusions and Summary

5.1 General Comments

The approach taken herein has proven to be a viable method to determine the constitutive parameters of a medium using noninvasive techniques. There have not been reports in the literature of attempts to perform such constitutive parameter extraction other than in the form of passing comments [10]. The method presented here is based on sound theoretical bases. Some approximations and assumptions have been made in the analysis, e.g., that $\mu_1 = \mu_2 = \mu_0$, $\sigma_{wire} = \infty$, homogeneity of the ground, absence of reflected waves on the wire (effective infinite length), perturbations of the measured current distributions by the measuring system are minimal, and the calibration factors for the measuring system are accurate. The method, while not necessarily robust, has yielded valuable information regarding the characteristics of the ground pad and has uncovered some of the capabilities and shortcomings of the approach. Some comments will be included in a later section.

Since the test program was conducted in a one-week period which did not allow for repeats of the data acquisition/analysis process or even for modifications of the process given observations based on analysis of the data, improvements in the experimental setup to permit improved estimates of the constitutive parameters have not been possible Nonetheless, a reasonable representation of the constitutive parameters of the reinforced concrete pad in the LESLI facility at the Phillips Lab has been achieved.

The constitutive parameters determined by this process are to be used in a program where the realistic ground is to be part of a computer model used in code validation. The test object, a Boeing 757 parked on a reinforced concrete pad, has a fuselage which is seven or more feet above the ground and the test points, except for a top-mounted external blade antenna, are located internal to the fuselage. It has always been expected that the ground will have its most pronounced effect on the structure of the field illuminating the airplane and will most likely have little effect on secondary scattering where the illuminating wave impinges on the airplane, scatters, impinges on the ground, scatters, and impinges on the airplane (thus "perturbing" the illuminating field). In a full wave analysis, this separation or consideration of the order of scattering is not an issue. We only make these comments to reflect on the relative importance of the ground characteristics in the ultimate solution.

51

5.2 Data Summary

The experimental data in the form of current distributions on a wire over ground were collected over a frequency range from approximately 1 MHz to 1 GHz at 90 spatial points spaced at 30 cm intervals. Reasonably accurate estimates of attenuation and phase constants were obtained for frequencies between 10 MHz and 126 MHz. Below this range, the spatial extent of sampling did not permit accurate estimates of the attenuation constant while beyond this frequency range, the sampling density and the limited support of the transmission line mode did not permit accurate estimates of the phase and attenuation constants, respectively. Over the frequency range, the constants led to estimates of ε_r and σ which were "reasonable" and within the range of physical realizability. Outside the range, the estimates for the constitutive parameters were decidedly less reliable. The estimates from the reliable range were used in a least squares fit to the Debye equations to yield expressions for the constitutive parameters and their average values over range $\{f_1, f_2\}$:

$$\varepsilon_r = 4.2418 + 6.1943 / (1 + 1.129 \cdot 10^{-17} \cdot \omega^2)$$

$$\sigma = 4.416 \cdot 10^{-11} \cdot \omega / (1 + 1.354 \cdot 10^{-17} \cdot \omega^2)$$

$$< \varepsilon_r (f_1, f_2) > = 4.24 + 2.93 \cdot 10^8 \cdot [\tan^{-1}(2.11 \cdot 10^8 \cdot f_2) - \tan^{-1}(2.11 \cdot 10^8 \cdot f_1)] / (f_2 - f_1)$$

$$< \sigma (f_1, f_2) > = 2.595 \cdot 10^5 \cdot Ln[(1 + 5.29 \cdot 10^{-16} \cdot f_2^2) / (1 + 5.29 \cdot 10^{-16} \cdot f_1^2)] / (f_2 - f_1)$$

Analysis of the experimental data allowed the identification of areas where the displacement current effects dominated. Certainly, displacement current effects were dominant above 50 MHz and it was evident from the reflection coefficient analysis that it was effectively independent of conductivity above 50 MHz and effectively independent of frequency above 100 MHz. Thus concern regarding the conductivity was secondary as its impact would be felt only below 50 MHz.

5.3 Concerns and Suggested Future Work on the Process

As mentioned previously, time and operational constraints did not permit a more in-depth study of the constitutive parameters and the technique used for their determination. In the future, this technique deserves an extended investigation as it represents a viable method for noninvasive determination of ε_r and σ. Specifically, several issues should be carefully studied to assess their impact on accuracy. In the following, several suggestions are made for future uses of the method and several areas are recommended for study.

Spatial Sampling

Prior to testing, an analysis was executed to bound the sampling density required to get reliable data over the interval 10 MHz to 400 MHz subject to the operational constraints of time and equipment availability. At the low frequencies it was anticipated that the difficulties would arise from the total attenuation that would be experienced over the entire sampling range. At the high frequencies it was expected that the difficulty would arise from the length of the interval over which the transmission line mode was dominant and the number of samples in this interval. In both cases the accuracy of the measurement system was a concern as was its dynamic range. While relative measurements ($I(x)/I(x_0)$) were adequate for our purposes, the system was limited by its inability to make accurate measurements of either component below -80 dBm or thereabouts. It was originally felt that sampling at four samples per wavelength was adequate so that the method could produce high quality results at 250 MHz at a sample spacing of 30 cm. Also, the total sampling range was 26.7 meters and it was estimated that sampling over a wavelength at low frequencies (approximately 11 MHz) would be adequate to assess the attenuation constant. In the presence of noise, reflections, and other fluctuations in the current distribution, the determination of attenuation constant at low frequencies was difficult. The attenuation observed over the entire sampling range was small. At high frequencies, these problems were compounded by the small interval over which the transmission line mode was dominant, the dynamic range of the measurement system, and the small number of samples per wavelength .

In future exercises, it would be beneficial to start the sampling closer to the source to increase the reference signal level and to maximize the length over which the transmission line mode dominates. This will help to extend the high frequency limit. Also, the sampling density should be increased in the high frequency regime in order to generate more samples per wavelength. For the low frequency range, the length over which sampling takes place should be made as large as possible so that the current is sampled over several wavelengths. In the face of limited resources, rather than having uniform sampling over the entire measurement range, it will be beneficial to sample more densely near the source for high frequency coverage and less densely for low frequency coverage. This suggests a nonuniform sampling scheme and may imply a logarithmic sampling rate with more density near the source and less farther away.

Reflections

The presence of reflections on the line must be minimized. The current distribution must be entirely that of a transmission line mode on an infinite line. The extraction of reflected waves from unknown locations could make the process difficult if not impossible. Proper loading of finite length lines or sufficient length could make this issue insignificant.

Height

At present the impact of uncertainties on the accuracy of parameter estimates is unknown, in detail. Certainly the uncertainties here (plus or minus 1/8" at a height of 5/8") have not caused major difficulties but the overall impact should be studied.

System Effects

The effects of the measurement probes, e.g., the current probes and their cables, on the accuracy of the current distribution measurement should be looked at in detail.

Mathematical Issues

The process, which is a classical inversion problem, may not be robust. Small errors in α and β could lead to significant errors in ε_r and σ although such problems were not overwhelming in this case. This aspect should be studied to lend a measure of usefulness to this technique. In the range of displacement current domination, when a consistent solution may not be available because of great uncertainties in σ due to its limited impact on the current distribution, are there methods to obtain reasonable estimates of ε_r which would suffice? Are alternate methods available? Likewise, similar questions must be answered for the case when conduction current dominates.

References

1) Robert L. Baker and Felix L. Pitts, eds., "Fly-by-Light/Power-by-Wire Requirements and Technology Workshop," NASA CP-10108, September 1992.

2) D. C. Chang and R. G. Olsen, "Excitation of an Infinite Antenna Above a Dissipative Earth," *Radio Science*, Vol. 10, No. 8,9, pp. 823-831, August-September 1975.

3) E. F. Kuester, D. C. Chang and R. G. Olsen, "Modal Theory of Long Horizontal Wire Structures Above the Earth, 2, Properties of Discrete Modes," *Radio Science*, Vol. 13, No. 4, pp. 615-623, July-August 1978.

4) R. G. Olsen, E. F. Kuester and D. C. Chang, "Modal Theory of Long Horizontal Wire Structures Above the Earth, 1, Excitation," *Radio Science*, Vol. 13, No. 4, pp. 605-613, July-August 1978.

5) G. J. Burke, "A Comparison of Solutions for Wires Over Ground", 8th Annual Review of Progress in Applied Computational Electromagnetics, 16-20 March, 1992.

6) G. J. Burke and A. J. Poggio, "Numerical Elecromagnetics Code (NEC) - Method of Moments" Lawrence Livermore National Laboratory, Rept. UCID - 18834, January 1981.

7) R. W. P. King and G. S. Smith, Antennas in Matter, MIT Press, 1981

8) R. S. Elliott, Electromagnetics, McGraw-Hill, 1966

9) C. Kittel, Quantum Theory of Solids, John Wiley, 1963

10) B. Rama Rao and D. N. Jones, "Characterization of a High Frequency Beverage Antenna Using a Fiber-Optic Measurement Technique", Antennas and Propagation Symposium, June 24 - 28, 1991, London, Ontario

REPORT DOCUMENTATION PAGE

Public reporting burden for this collection of information is estimated to average 1 hour per response, including the time for reviewing instructions, searching existing data sources, gathering and maintaining the data needed, and completing and reviewing the collection of information. Send comments regarding this burden estimate or any other aspect of this collection of information, including suggestions for reducing this burden, to Washington Headquarters Services, Directorate for Information Operations and Reports, 1215 Jefferson Davis Highway, Suite 1204, Arlington, VA 22202-4302, and to the Office of Management and Budget, Paperwork Reduction Project (0704-0188), Washington, DC 20503.

1. AGENCY USE ONLY (Leave blank)	2. REPORT DATE	3. REPORT TYPE AND DATES COVERED
	June 1995	Contractor Report

4. TITLE AND SUBTITLE

The Determination of the Constitutive Parameters of a Medium With Application to a Reinforced Concrete Pad

5. FUNDING NUMBERS

PO L-79902C

WU 538-01-13-01

6. AUTHOR(S)

A. J. Poggio, G. J. Burke, and S. T. Pennock

7. PERFORMING ORGANIZATION NAME(S) AND ADDRESS(ES)

Lawrence Livermore National Laboratory
University of California
Livermore, CA 94551

8. PERFORMING ORGANIZATION REPORT NUMBER

UCRL-CR-120519

9. SPONSORING / MONITORING AGENCY NAME(S) AND ADDRESS(ES)

National Aeronautics and Space Administration
Langley Research Center
Hampton, VA 23681-0001

10. SPONSORING / MONITORING AGENCY REPORT NUMBER

NASA CR-4674

11. SUPPLEMENTARY NOTES

Langley Technical Monitor: Karl J. Moeller

12a. DISTRIBUTION / AVAILABILITY STATEMENT

Unclassified - Unlimited
Subject Category 33

12b. DISTRIBUTION CODE

13. ABSTRACT (Maximum 200 words)

This report describes the experimental and analytical efforts performed to determine the constitutive parameters of a reinforced concrete pad on which an aircraft (the NASA Boeing 757) was parked while it is internal electromagnetic environment was measured. This concrete pad is part of the Large Electromagnetic System-Level Illuminator (LESLI) test facility at the Phillips Laboratory, Kirtland Air Force Base, New Mexico. The relative dielectric constant, conductivity, index of refraction, and reflection coefficient have been determined over the frequency range of 0 to 300 MHz and are presented herein.

14. SUBJECT TERMS

Constitutive parameters; dielectric constant, permittivity; index of refraction; and remote sensing

15. NUMBER OF PAGES

56

16. PRICE CODE

A04

17. SECURITY CLASSIFICATION OF REPORT	18. SECURITY CLASSIFICATION OF THIS PAGE	19. SECURITY CLASSIFICATION OF ABSTRACT	20. LIMITATION OF ABSTRACT
Unclassified	Unclassified		